NanoRound: A benchmark study on the numerical approach in nanofluids' simulation

Alina Adriana Minea[a,*], Bernardo Buonomo[b], Jonas Burggraf[c], Davide Ercole[b],
Kavien Raaj Karpaiya[c], Anna Di Pasqua[b], Ghofrane Sekrani[d], Jan Steffens[c], Jan Tibaut[e],
Niklas Wichmann[c], Peter Farber[c], Angel Huminic[f], Gabriela Huminic[f], Razvan Mahu[g],
Oronzio Manca[b], Cristina Oprea[g], Sebastien Poncet[d], Jure Ravnik[e]

[a] Technical University "Gheorghe Asachi" from Iasi, Romania
[b] Dipartimento di Ingegneria, Università degli Studi della Campania "Luigi Vanvitelli", Via Roma 29, 81031 Aversa, CE, Italy
[c] Hochschule Niederrhein University of Applied Sciences, Krefeld, Germany
[d] Mechanical Engineering Department, Université de Sherbrooke, 2500 Boulevard de l'Université, Sherbrooke, QC J1K2R1, Canada
[e] Faculty of Mechanical Engineering, University of Maribor, Slovenia
[f] Transilvania University of Brasov, Romania
[g] Tensor SRL, Bucharest, Romania

ARTICLE INFO

ABSTRACT

Numerical simulation of nanofluid flows is of maximum importance for a large area of applications, especially in the solar energy technology. Even though a lot of numerical studies are available in the open literature, there is still a large debate in regard to the most appropriate approach when dealing with nanofluids. Plus, a precise simulation of the thermal fluid-solid system encompasses a profound understanding of the fundamental physical phenomena that appear in the nanofluid flow. In this idea, a number of simplifications and approaches are considered, and the aim of this benchmark study is to shed some light in the most suitable CFD approach when dealing with nanofluid flow.

Finally, different approaches were considered by different research groups with relevant experience in CFD and are discussed accordingly and in connection with an experimental case that was chosen as a comparison. The current benchmark study was projected to be an ample reference for investigators interested in dealing with the numerical study of the nanofluids' flow.

1. Introduction

By definition, a round robin test is an interlaboratory test (measurement, analysis, or experiment) performed independently several times. This can involve multiple independent scientists performing the test, with the use of the same method in different equipment, or a variety of methods and equipment. In reality, it is often a combination of the two, for example, if a sample is analysed, or one (or more) of its properties is measured by different laboratories using different methods, or even just by different units of equipment of identical construction.

Engineered suspensions of nanoparticles in fluids, acknowledged as "nanofluids," have created significant interest for their potential to boost the convective heat transfer rate in most engineering systems, while loweringthe problems of erosion, sedimentation and clogging that were acknowledged for colloids or other fluid mixtures with solid particles [1–12]. The idea of Round Robin tests is not new in the literature, and some tests related to nanofluids' behaviour were also performed, especially on thermal conductivity measurements [13,14]. On the other hand, according to Google Scholar, in 2018 there were only about 9080 nanofluid-related publications in different journals, including patents, and an increase is estimated in this area of research. Besides, a lot of review papers on nanofluid heat transfer [1–8] have been published, and even some books completely devoted to nanofluids [9–12] are noticed in the archived databases.

Even if a lot of research is noticed in the nanofluids' area, some drawbacks were noticed, and this can delay their technology readiness level increase [15–18]. One of these drawbacks is related to the actual energy performance versus price for nanofluids, and Alirezaie et al. [15] discussed the efficiency-price index over the few already studied

---

nanofluids (i.e. four nanofluids based on water). They concluded that, even though the properties are indicating a good energy efficiency, the price does not justify the use of nanofluids for basic real life applications.

Another drawback is the insufficient discussion on the performance analysis in real life test cases. Xu et al. [16] discuss the convective heat transfer analytically for three main cases: Nanofluid in a plain tube, base-fluid in a foam metal tube, and nanofluid in a metal-foam tube. It was found that the Nusselt number first increases and then decreases with an increase in nanoparticle concentration, while the Nusselt number of the nanofluid in a metal-foam tube diminishes with an up-surge in ratio of Brownian to thermophoretic diffusivities.

Forced convective heat transfer of nanofluids in a metal-foam duct was investigated numerically by Xu et al. [17], and the main conclusion was that the field synergy principle for pure fluid convection cannot guide the analysis of the heat transfer enhancement for nanofluid in metal foams. This observation requires modification of the existing field synergy principle to be applicable to nanofluids. Moreover, nanofluid heat transfer enhancement cannot balance the pressure drop increase.

Despite the overwhelming attention received by these new nano-particles enhanced fluids, there are still some drawbacks in the nano-fluids research, and one of them is related to their numerical approach (see also references [3, 16–23]). The debate in the literature about existing models and what is the most appropriate one remains tangible [16–23]. A useful review was accomplished by Kamyar et al. [23] which summarised a number of numerical studies achieved in nano-fluids' simulation, including conservative numerical methods, as well as non-conventional approaches. They concluded that most of the results were in tolerable agreement with the experimental outcomes, and mathematical models' changes might be necessary, such as using two-phase models instead of single-phase models for nanofluids. Other comprehensive studies on modelling and simulation of nanofluid flows were published recently by Mahian et al. [24,25], who acknowledged the gaps in the simulation approaches and discussed them in detail, along with some recommendations for future research. The two ample assessments [24,25] were submitted in two parts, first about the fundamentals and theory, and the second one revising the applications of nanofluid flow.
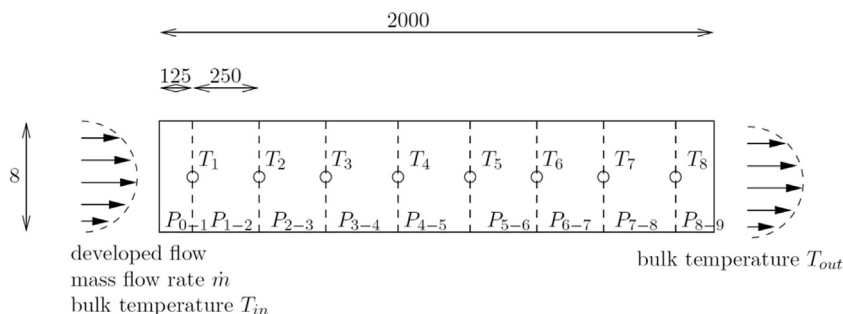
Fig. 1. A sketch of the test case.

In this idea, these authors considered that a unified and systematic approach will be of top interest for researchers in the area of Nanofluids. Consequently, the objectives of this study are to conduct a round robin test on numerical approaches of nanofluids, and compare the numerical results with the experimental ones, as will be detailed in the next section. Plus, a selection of different approaches will be used by different research groups, while a comparison will be delivered on the accuracy of each approach.

2. Nanoround methodology and validation basis

The nanoround project idea is a result of several working groups on CFD (Computational Fluid Dynamics) applied to nanofluids, and attempts in finding the best way to describe a nanofluid flow numerically. Its validation relies on a sophisticated experimental study performed by Colla et al. [26]. This particular work was chosen as a reference due to its accurate measurements, as well as the multitude of checkpoints.

Briefly, in Fig. 1 is depicted a scheme of the experiment, where four power/mass flux combinations were chosen. Placement of temperature sensors is also depicted, and all dimensions are in *mm*. Therefore, pipe length is 2 *m*, pipe inner diameter is *d* = 8 *mm*, pipe outer diameter is *12 mm*. The test cases are denoted: 100-6, 100-8, 200-5, 200-6, and detailed information is given in Appendix A. There are nine heating elements along the pipe surface with different heat flux. Temperature was measured at eight locations. At each location four sensors were installed, located at the top, bottom and at the two sides of the pipe.

2.1. Boundary conditions for test cases

The simulation domain is composed from a solid and fluid parts. The solid part is the pipe, which is a copper cylinder of length 2 *m*, inner diameter 8 *mm,* outer diameter *12 mm*. The fluid part is a cylinder of length 2 *m* and diameter 8 *mm*. A developed flow with constant temperature enters the test section. Heat flux along the length of the pipe has been measured, and is used as a boundary condition. The results of simulation are temperatures at 8 locations along the wall, which have also been measured experimentally. The measured temperature is given by the average of 4 sensors placed around the circumference of the pipe (one on the top, one left, one right and one at the bottom).

Two domains should be simulated: A solid and a fluid domain. Heat conduction in the solid pipe and nanofluid flow, and heat transport in the fluid domain. Temperature differences in the fluid give rise to buoyancy forces, which must also be taken into account.

Boundary conditions can be outlined as:

- *momentum conservation in the fluid domain*
  - at the inlet: A developed velocity profile; prior simulation is necessary to estimate the profile and/or an analytical solution could be used,
  - at the wall: A no-slip boundary condition (flow velocity is zero)
  - at the outlet: A constant static pressure is known. Can be chosen arbitrarily, i.e. relative pressure is zero
- *energy conservation in the fluid domain*
  - at the inlet: A constant temperature is known
  - at the wall: Heat flux into the solid domain is conserved
  - at the outlet: Not necessary, i.e. convective outflow boundary condition is used
- *energy conservation in the solid domain*
  - at the inlet: Zero heat flux
  - at the wall: Heat flux into the solid domain is known from the experimental data
  - at the outlet: Zero heat flux

2.2. Properties of nanofluids: TiO_2 - water

Colla et al. [26] used two concentrations of TiO_2 – water nanofluid:

1.0 wt% and 2.5 wt%. for their experiment. The TiO_2 water-based nanofluid was supplied by Sigma Aldrich at 35.0% by mass. *Bi*-distilled water (Carlo Erba, CAS Nr 7732-18-5) was employed to dilute the commercial nanofluid to obtain the desired concentrations of 1.0 wt% and 2.5 wt%. Starting from the fluid at 35.0 wt% after 1 h sonication, bi-distilled water was added in a weight amount, measured by an analytical balance (Gibertini E42S 240 g FS), with an uncertainty of ± 0.002 g. Each composition was further sonicated for 1 h in order to disperse the nanoparticles completely. Acetic acid was present as a dispersant at 1.0–5.0 wt% of the whole suspension.

The nanofluid concentration was evaluated by measuring the density of the nanofluid at 20 °C by means of a glass vibrating tube densimeter (Anton Paar DMA 602), assuming a linear dependence of density on the volumetric fraction of nanoparticles [26]. Density of titania is considered to be 3972 kg/m³.

Thermal conductivity (see the results in Table 2) was measured in a temperature range between 10 °C and 60 °C, employing a TPS 2500 S (Hot Disk®), an instrument based on the hot disk technique which can measure thermal conductivity and thermal diffusivity of several materials [26].

2.2.1. Density

Nanofluid densities are 1005.0 kg/m³ and 1016.4 kg/m³ for 1.0 wt% and 2.5 wt%, respectively. From that the actual TiO_2, mass fractions result to 1.06 wt% (0.27 vol%) and 2.54 wt% (0.65 vol%). All the following calculations were carried out employing these values. However, for simplicity, the nanofluids were still characterised with 1.0 wt% and 2.5 wt%.

2.2.2. Viscosity

A rotational rheometer (AR-G2, TA Instruments) was used to determine dynamic viscosity in a temperature range between 10 °C and 40 °C. All measurements were performed at constant temperature and shear rates ranging from 80 s^{-1} to 1200 s^{-1}, with a constant increment of 124 s^{-1}. Measurements were taken at a shear rate of 826 s^{-1}. The declared instrument uncertainty was 5.0% [26].

2.2.3. Specific heat

The nanofluid specific heat was measured by a Differential Scanning Calorimeter (DSC).

For the nanofluid at 2.5 wt%, specific heat was measured at a temperature of 31.8 °C and 71.8 °C. Experimental data were 4047.9 J/(kg K) and 4096.7 J/(kg K), respectively. A comparison between these results and the results from the average weight calculation confirm the validity of this model. Deviations were lower than the instrument uncertainty; therefore, heat capacity of 1.0 wt% nanofluid was calculated with the classical equation:

$$(c_p)_{nf} = \omega (c_p)_{np} + (1 - \omega)(c_p)_{bf} \tag{1}$$

3. Nanofluid models

3.1. Model 1 – the effective properties model

The simplest model used to simulate the flow of a nanofluid is to assume that the suspension of nanoparticles and fluid can be described by effective material properties - viscosity, thermal conductivity, density and specific heat capacity. Nanofluid density is modelled using a mixing rule based on the particle volume fraction φ. Let ρ_f be the base fluid density, and let ρ_s be the density of solid nanoparticles. With this, the nanofluid density can be written as

$$\rho_{nf} = (1 - \varphi)\rho_f + \varphi \rho_s \tag{2}$$

The apparent viscosity of the nanofluid suspension μ_{nf} is different from the base fluid viscosity μ_f, because of the inclusion of
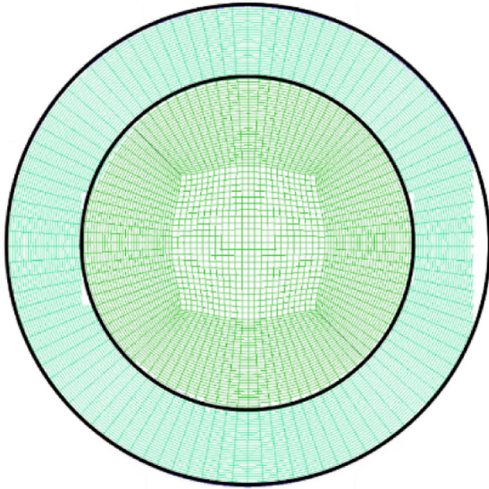
Fig. 2. Section of the tube, illustrating the meshed areas.

nanoparticles. Several approaches were proposed, aimed at estimating nanofluid viscosity. In this work, the Brinkman [28] formula was chosen, which is valid for ($\varphi < 0.04$), and it reads:

$$\frac{\mu_{nf}}{\mu_f} = (1 - \varphi)^{-2.5} \tag{3}$$

Khanafer et al. [29] proposed a mixture model for nanofluid heat capacity:

$$(\rho c_p)_{nf} = (1 - \varphi)(\rho c_p)_f + \varphi(\rho c_p)_s \tag{4}$$

The same idea can be employed for thermal expansion coefficient: $(\rho\beta)_{nf} = (1 - \varphi)(\rho\beta)_f + \varphi(\rho\beta)_s$. When the definition of ρ_{nf} is taken into account, we can write:

$$\beta_{nf} = \beta_f \left[\frac{1}{1 + \frac{(1-\varphi)\rho_f}{\varphi\rho_s}} \frac{\beta_s}{\beta_f} + \frac{1}{1 + \frac{\varphi}{1-\varphi}\frac{\rho_s}{\rho_f}} \right] \tag{5}$$

The Maxwell-Garnett formula [30] can be used to estimate the effective thermal conductivity of the nanofluid:

$$k_{nf} = k_f \frac{k_s + 2k_f - 2\varphi(k_f - k_s)}{k_s + 2k_f + \varphi(k_f - k_s)} \tag{6}$$

This expression assumes that the particles are spherical, and it is applicable for small temperature gradients.
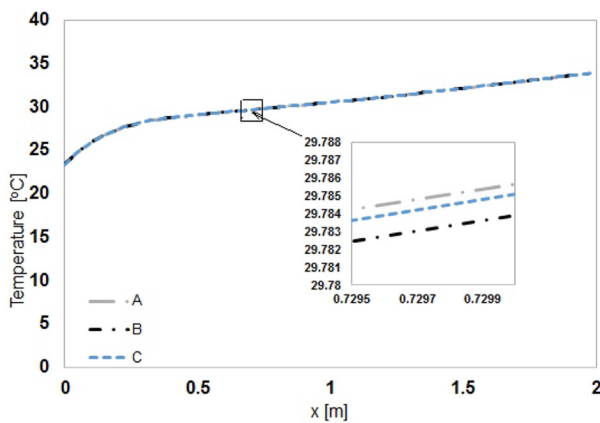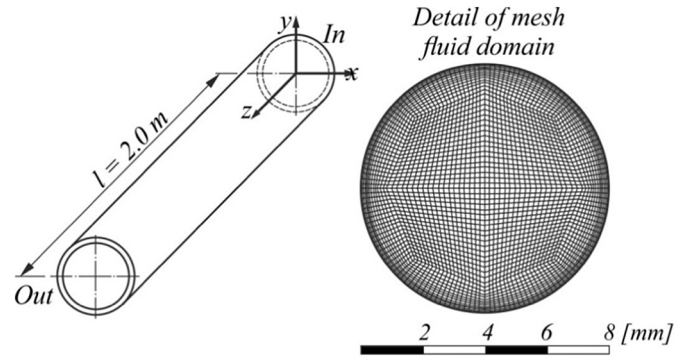
Fig. 4. Mesh for test case B and C.

3.2. Model 2 – the mixture model

The effective properties model assumes that the particle distribution is uniform throughout the whole flow field regardless of the flow conditions and temperature. This assumption is supported by the fact that the particle Stokes number (the ratio of the particle response time scale and the characteristic flow relaxation time scale) is very low. With a very short response time a nanoparticle is able to follow the fluid exactly, and due to the huge number of particles involved, the assumption of effective properties seems reasonable. However, experimental studies (Wen and Ding [31]) have shown that the single-phase effective properties model may not be always applicable. They found that the distribution of particles is non-uniform, and that the lower concentration of particles close to the walls leads to lower heat transfer rates. One possible reason for the fact that the particles do not follow the fluid could be that there is a slip between the flow and the particle velocity.

Buongiorno [32] considered several mechanisms. The first mechanism is the Brownian diffusion, numerous collisions of nanoparticles and the base fluid molecules in random-like motion. If we consider nanoparticles as large fluid molecules with average kinetic energy $\frac{1}{2k_B T}$, we can use the Stokes-Einstein equation for Brownian diffusivity

$$D_B = \frac{k_B T}{3\pi\mu d_p}, \tag{7}$$

where the Boltzmann constant is denoted by k_B. The resulting nanoparticle mass flux may be modelled using a Fickian gradient hypothesis yielding

$$\vec{j}_B = -\rho_p D_B \nabla\varphi \tag{8}$$

A nanoparticle also exhibits diffusion due to the temperature
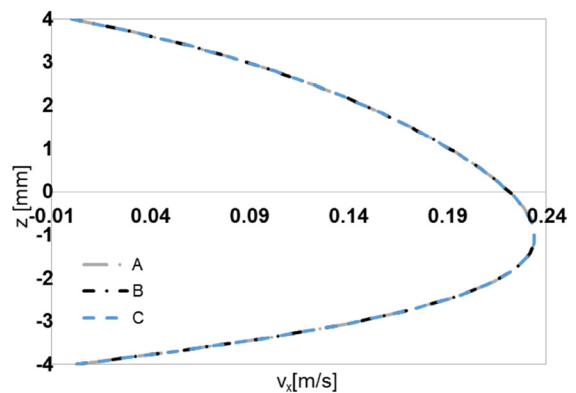
Fig. 3. Comparison of streamwise (a) and spanwise (b) at x = 1.875 m temperature and flow profiles obtained using three grids.
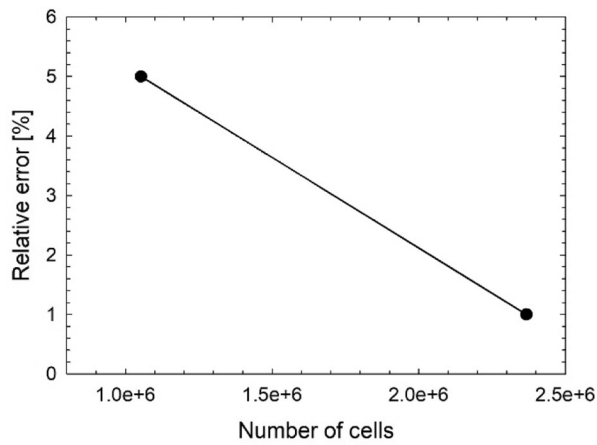
a.
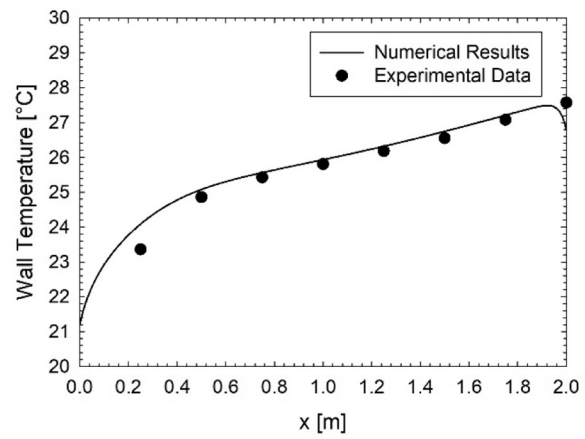
b.

Fig. 5. Independence and validation of Test E: (a) Mesh independence test and (b) Validation test.
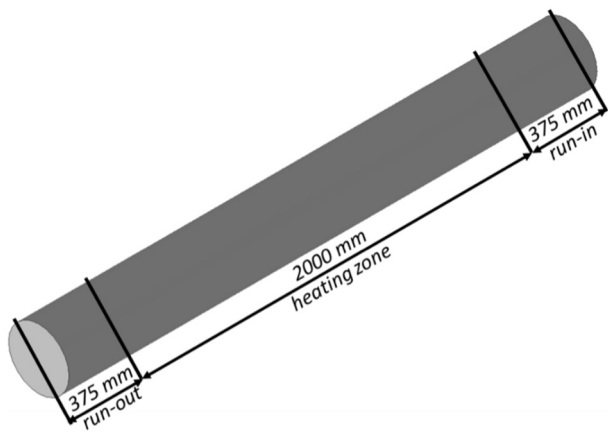
Fig. 6. Simulation setup and boundary conditions.
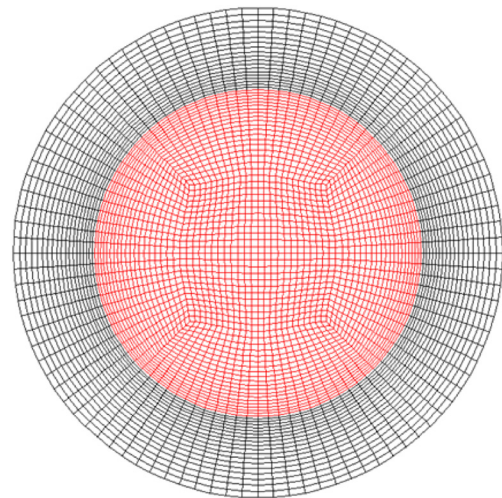
Fig. 8. Front view of o-grid mesh with meshed wall.
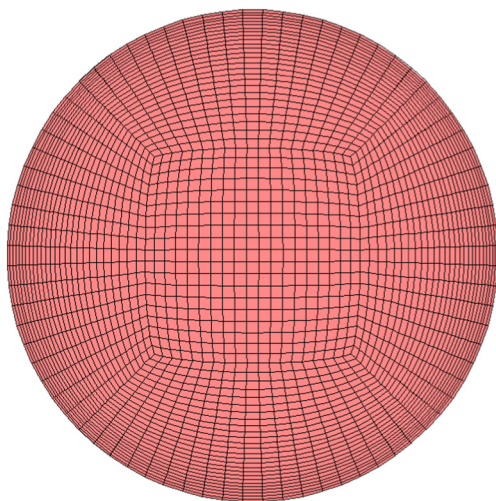
Fig. 7. Front view of o-grid mesh with shell conduction.

Fig. 9. Development of the temperature field along the length of the pipe.

gradient in the fluid. This effect is called thermophoresis, and can be modelled by the introduction of the thermophoretic nanoparticle mass flux

$$\vec{j_T} = -\rho_p D_T \frac{\nabla T}{T}, \quad D_T = \beta \frac{\mu}{\rho_f} \varphi, \tag{9}$$

where $\beta = 0.26 k_f / (2k_f + k_p)$ ([32]).

The mixture model considers the nanofluid to be a two-component mixture of nanoparticles and the base fluid. We have identified two diffusive mechanisms which govern the nanoparticle motion relative to
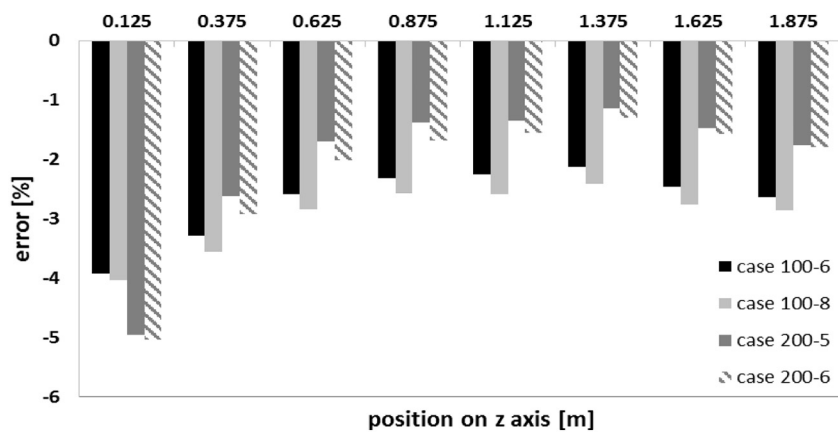
Fig. 10. Errors' analysis.
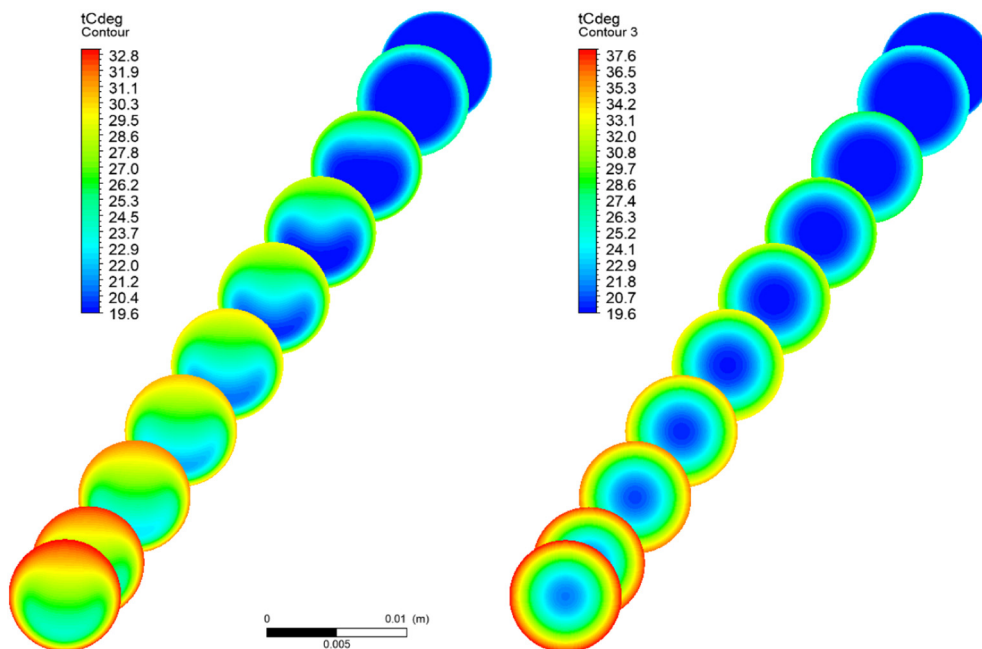
Fig. 11. Temperature's variation in the cross-sections of the tube, case $P = 100$ W, mass flow rate = 6 g/s, gravity on (left) and gravity off (right).
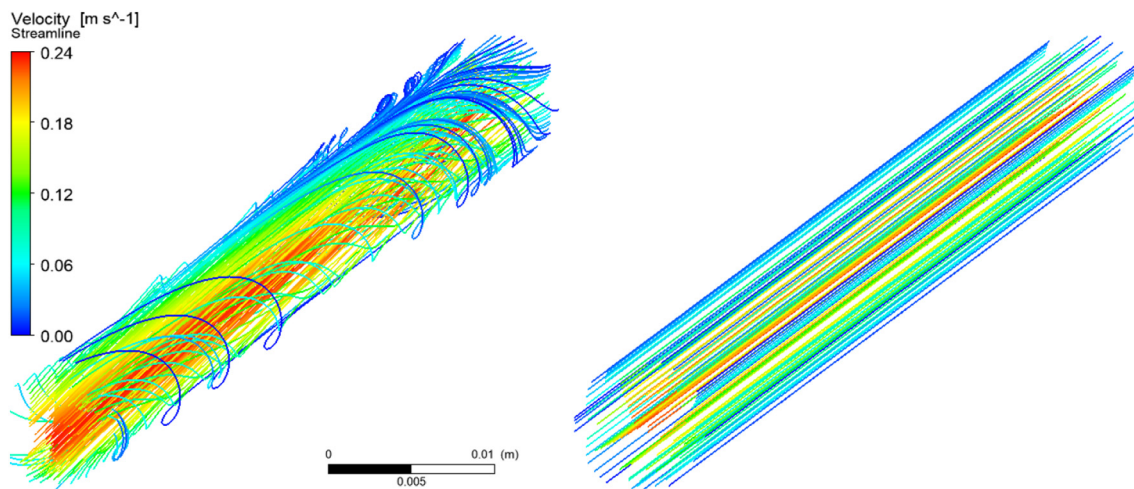
Fig. 12. Streamlines, case P = 100 W, mass flow rate = 6 g/s, gravity on (left) and gravity off (right).
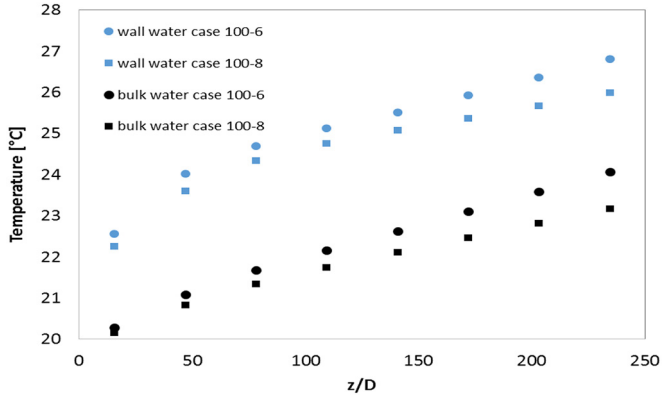
Fig. 13. Effect of the mass flow rate on the temperature axial distributions of water. Full symbols stand for wall temperature and empty symbols for bulk temperature.

the flow velocity. We may use them to write the nanoparticle concentration transport equation. Realising that accumulation of nanoparticles in a control volume can be caused by convective or diffusive transport, we can write the following transport equation

$$\frac{\partial \varphi}{\partial t} + (\vec{u} \cdot \nabla)\varphi = -\nabla \cdot (\vec{j_B} + \vec{j_T}) \tag{10}$$

Introducing Brownian (8) and thermophoretic (9) mass fluxes it arrives at:

$$\frac{\partial \varphi}{\partial t} + (\vec{u} \cdot \nabla)\varphi = \nabla \cdot \left(D_B \nabla \varphi + D_T \frac{\nabla T}{T} \right) \tag{11}$$

The energy conservation equation for the nanofluid needs to be adapted to include the added heat flux due to the changing particle concentration:

$$\rho c_p \left(\frac{\partial T}{\partial t} + \vec{u} \cdot \nabla T \right) = -\nabla \cdot (-k\nabla T + c_p T(\vec{j_B} + \vec{j_T})) + c_{p,p} T \nabla \cdot (\vec{j_B} + \vec{j_T}), \tag{12}$$

where the heat capacity of the nanofluid is denoted by c_p, $c_{p,\,p}$ is the heat capacity of particles and k is the thermal conductivity. This simplifies to

$$\rho c_p \left(\frac{\partial T}{\partial t} + \vec{u} \cdot \nabla T \right) = \nabla \cdot (k\nabla T) - c_{p,p}(\vec{j_B} + \vec{j_T}) \cdot \nabla T, \tag{13}$$

where we took $\nabla(c_{p,\,p}T) = c_{p,\,p}\nabla T$ due to the assumption of thermal equilibrium between the fluid and particles. Inserting the Brownian and thermophoretic heat fluxes into the equation gives

$$\rho c_p \left(\frac{\partial T}{\partial t} + \vec{u} \cdot \nabla T \right) = \nabla \cdot (k\nabla T) + \rho_p c_{p,p} \left(D_B \nabla \varphi \cdot \nabla T + D_T \frac{\nabla T \cdot \nabla T}{T} \right), \tag{14}$$

which is the final form of energy conservation equation.

4. Numerical tests' validation

4.1. Tests details

The numerical approach was divided between different research groups, as seen in Table 3.

For most of the natural-convection flows, faster convergence can be obtained using the Boussinesq model, available in most of the commercial CFD codes. This model treats density as a constant value in all solved equations, except for the buoyancy term in the momentum equation:

$$(\rho - \rho_0)g \simeq -\rho_0 \beta (T - T_0)g \tag{15}$$

where ρ_0 is the (constant) density of the fluid, T_0 is the operating temperature, and β is the thermal expansion coefficient.

The Boussinesq model can be used successfully for incompressible flows, and in the cases where the density variation is driven by small temperature variations (i.e.: $< 10\,°C$ at a given cross-section for water based fluids). Nevertheless, as limitations, the Boussinesq model should not be used if the temperature differences in the domain are large, which is not the case, as can be seen clearly from Annex 1. In this regard, the natural convection flow was approached using the Boussinesq model for test cases A - E.

4.2. Mesh validation

Each group used its own mesh and validated for water flow in the designed configuration.

4.2.1. Test A

We considered pure water simulations, effective properties model (model 1) and mixture model (model 2) with homogenous and inhomogeneous inlet boundary conditions. Three grid designs (Fig. 2) were considered: Grid A: 3.6 million, grid B: 11 million and grid C: 16 million nodes. Flow profiles for the pure water case were compared (Fig. 3), and since only small differences between grids were noticed, it was decided that all simulation would be performed on the 11 million nodes grid.

4.2.2. Test B and Test C mesh

Based on previous studies [33,34], the grid of the computational domain was generated using a multi-block scheme with hexahedral elements, as shown in the Figure below for the case of the fluid (water) domain. The total number of generated cells was 1,368,000 for the fluid domain and 304,000 for the solid domain.

4.2.3. Test D

To validate the numerical results, two sets of simulation were

| (a) | (b) | (c) |
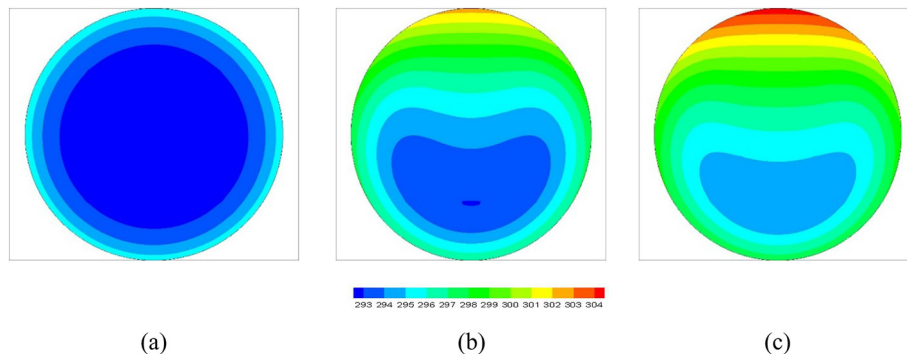
Fig. 14. Maps of temperature T at three axial positions: (a) z = 0.125 m, (b) z = 1.125 m and (c) z = 1.875 m for W-100-6 case.
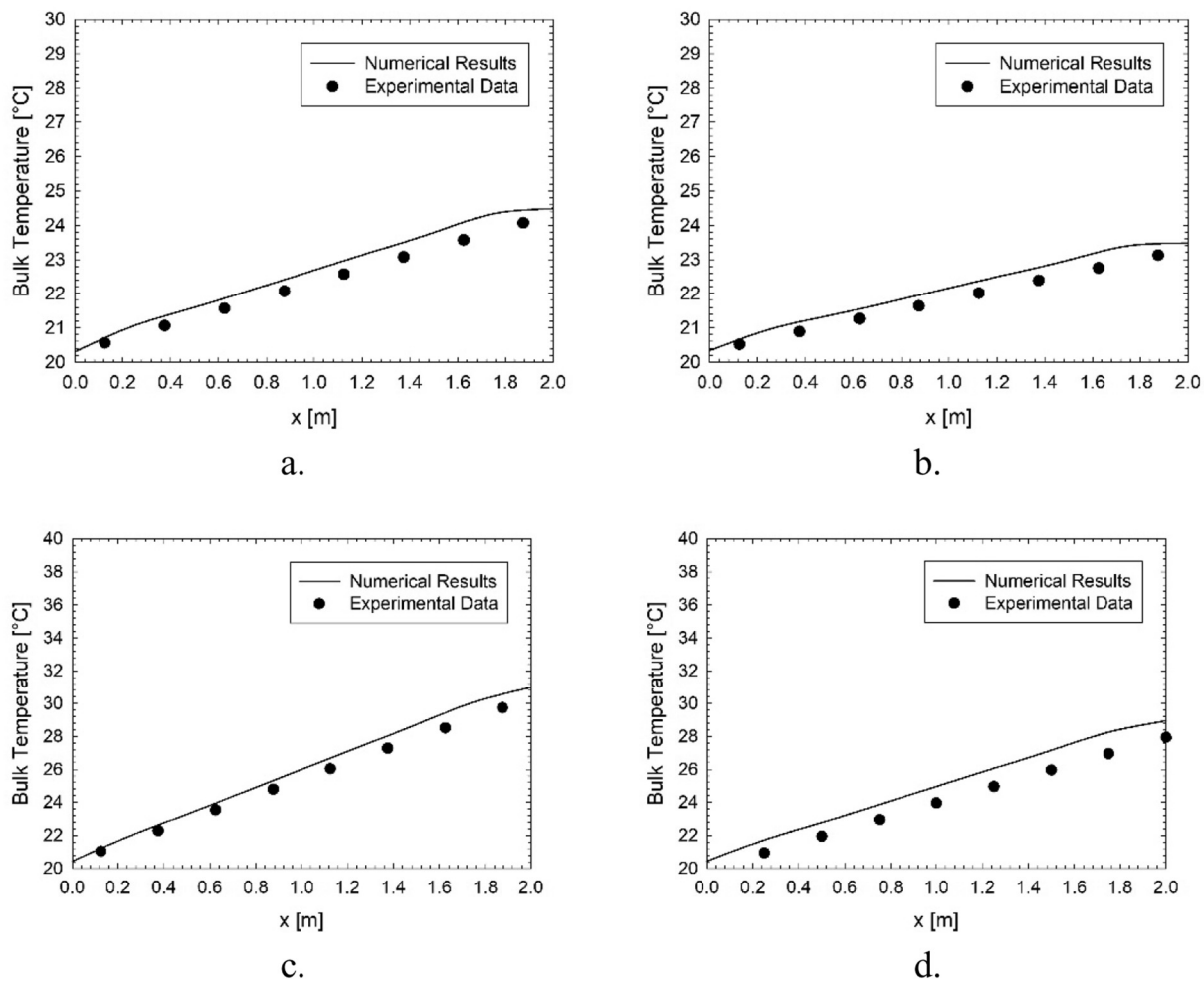
Fig. 15. Comparison with water in terms of bulk temperature for different cases: (a) 100-6, (b) 100-8, (c) 200-5 and (d) 200-6.

considered, with and without the shell conduction within the pipe wall. The W-200-6 case was used for the grid independency analysis. Five structured grids were tested with 4, 6, 8, 17 and 53 million nodes, which consisted of 5365, 7077, 7885, 9557 and 10,725 nodes in the cross-section and 800, 920, 1100, 1820 and 5000 nodes along the axial direction, respectively. A mesh refinement close to the pipe wall was performed in order to capture the development of the boundary layer. The mesh growth rate was fixed at 1.1 for all the tested grids. The mesh was constructed under the Ansys ICEM. The prediction of the wall and bulk temperatures for the case with shell conduction are compared in Table 4.

From Table 4, a small difference of about 1% is obtained between the thinnest (53 million nodes) and the coarsest (4 million nodes) grids, whatever the axial positions. The numerical values are not in satisfactory agreement with the experimental data, with discrepancies between 6% and 30% in terms of both wall and bulk temperatures. The main conclusion is that mesh composed of 4 million nodes is sufficient to get grid independent results.

The same grid independence study has also been confirmed for the case without the shell conduction (results not shown here for the sake of brevity) leading to a similar conclusion. Thus, the 6 million nodes mesh grid, which offers the best overall compromise between accuracy and computational efforts, will be used in all the simulations presented hereafter. One will also see in the following sections that not accounting for the shell conduction improves the numerical predictions considerably.

4.2.4. Test E

The finite volume method was used to discretize the set of nonlinear equations. The SIMPLE algorithm was employed for the pressure-velocity coupling. A second order scheme algorithm was used for the pressure calculation, and a second order upwind scheme for energy and momentum calculation. The residuals are, respectively, assumed equals to 10^{-4} and 10^{-8} for continuity, momentum equation and energy equation. The numerical grid is a set of quadrilateral cells, having a small size near the boundary and a large size in the centre of the grid near the axis.

In order to check the accuracy of the results, a grid independency test was made with 3 different sizes: 1053024, 2,367,308, 5,875,231. The different results are compared in Fig. 5. A grid with 2,367,308 cells was chosen to perform the study, because the relative error is minor, of 1%, and therefore it represents the best compromise between the computational costs and accuracy. This numerical grid was also compared with the experimental results in terms of Wall temperature for the case of 100–6 (100 W of thermal power with 6 g/s of mass flow rate). The mean deviation from experimental results is 0.5% and it is shown in Fig. 5b.

4.2.5. Test F

The mesh of the present pipe geometry was built with the ANSYS ICEM 18.2. An o-grid seen in Fig. 6 was created, and refined gradually in every spatial direction. The refinement through the boundary layer was set to 5%. Four different cases were tested to achieve a very slight deviation between the experiments and the CFD simulations:
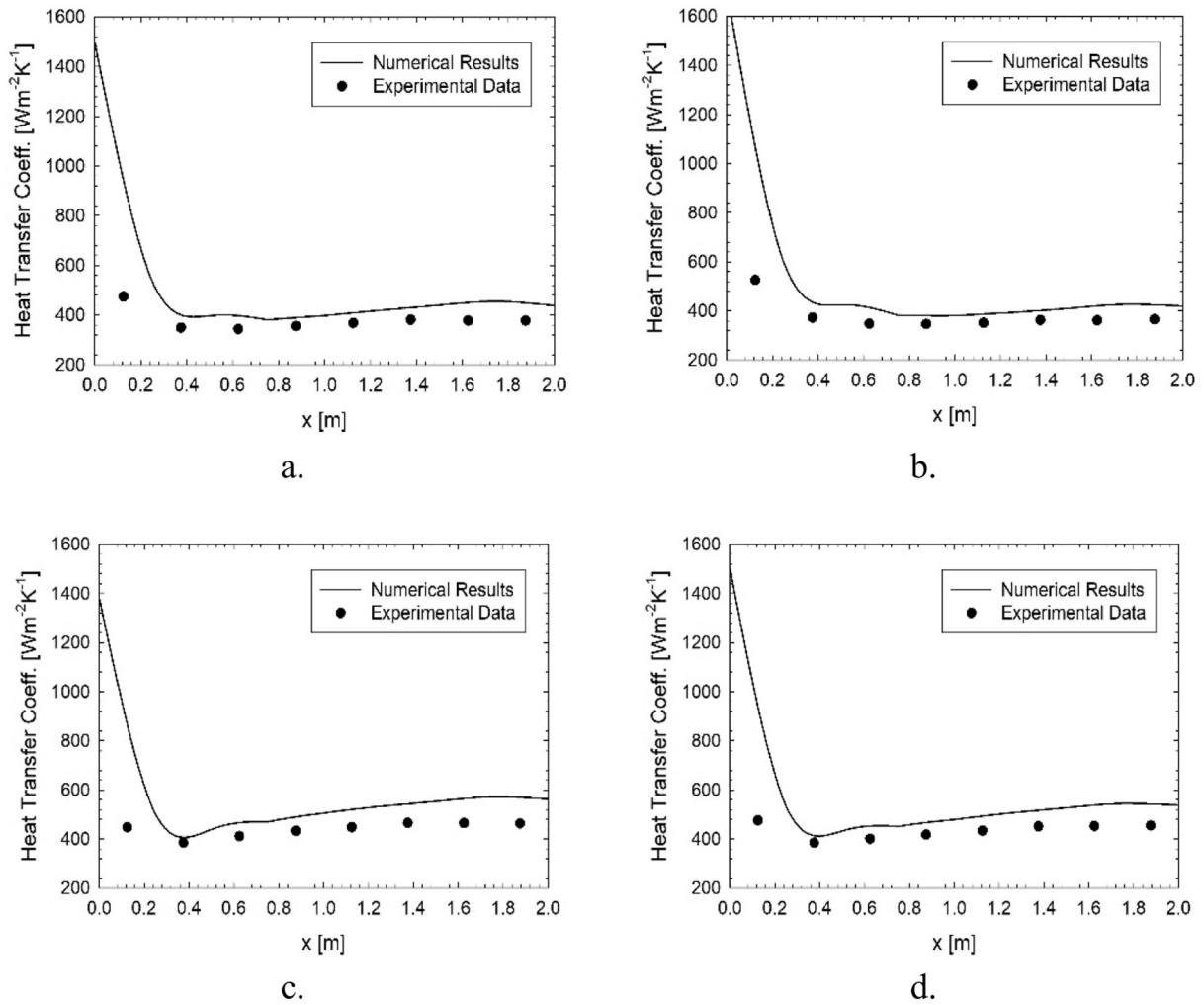
Fig. 16. Comparison with water in terms of h number for different cases: (a) 100-6, (b) 100-8, (c) 200-5 and (d) 200-6.
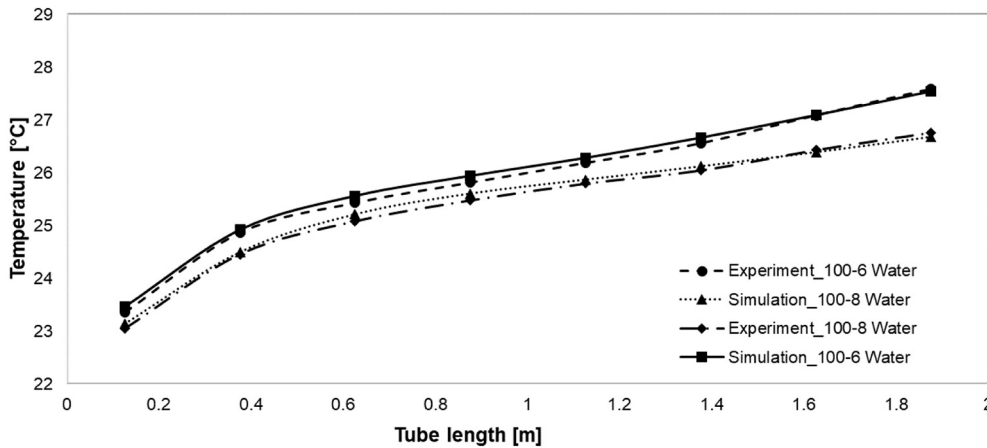
Fig. 17. Comparison of the simulation and experimental wall temperatures by Q = 100 W.

- with shell conduction / without run-out.
- with shell conduction / with run-out.
- with meshed wall / without run-out.
- with meshed wall/ with run-out.

The first differentiation between the different cases is the addition of a run-out as shown in Fig. 6. At this point, a pipe section with a length of 375 mm was added at the end of the heating zone.

Secondly, there, we distinguished between shell conduction and meshed wall. For the use of shell conduction only the volume of the fluid must be meshed. This leads to a single o-grid, as seen at Fig. 7.

The other case, where the copper wall is meshed separately in ICEM, is shown in Fig. 8. The refinement through the boundary layers between fluid and wall was also set to 5%.

Because of difficulties in matching the experimental data, different geometric designs were tested, and also a different set of equations for
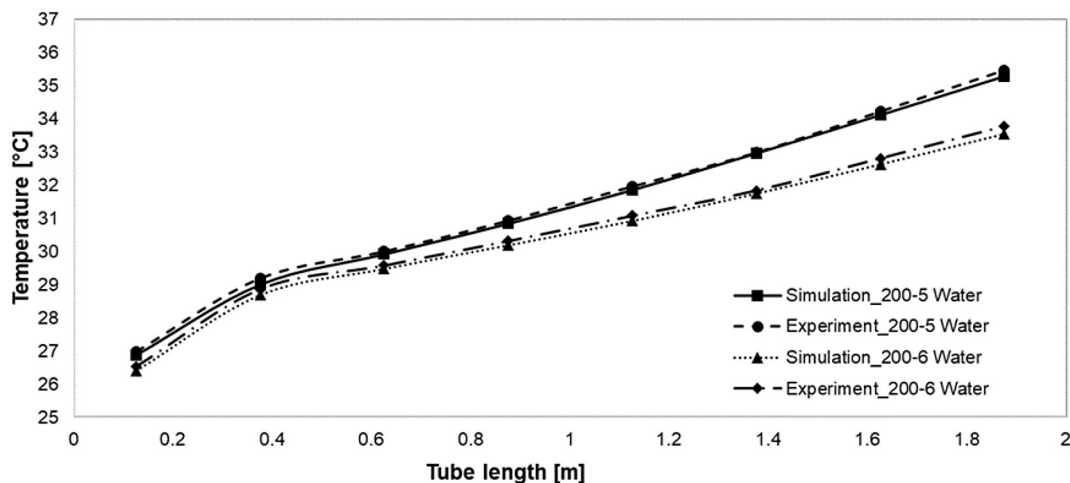
Fig. 18. Comparison of the simulation and experimental wall temperatures by Q = 200 W.

a.

b.
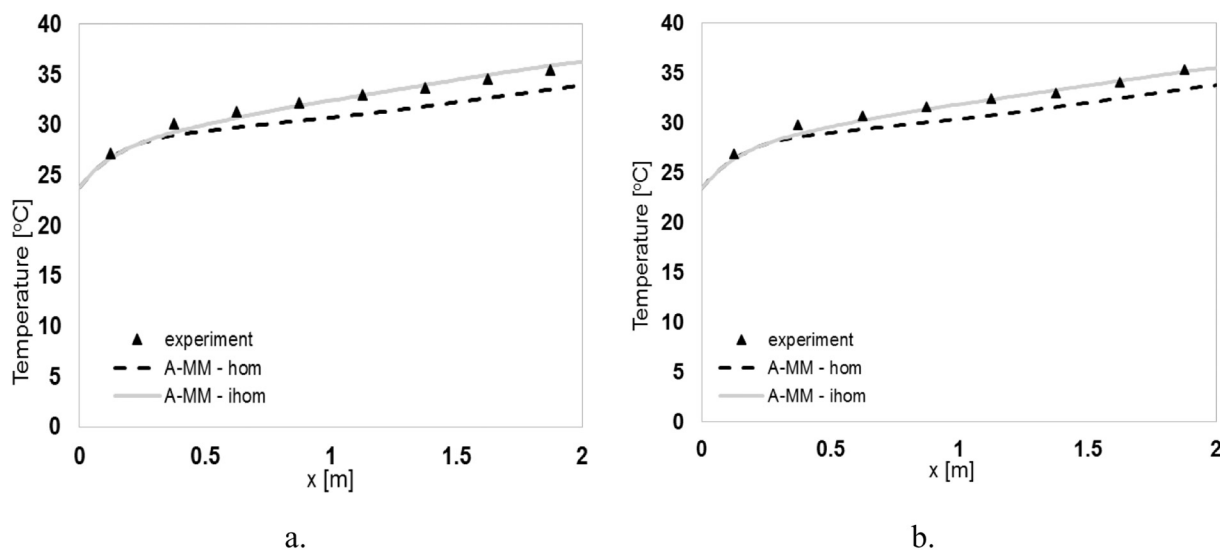
Fig. 19. Temperature profiles along the wall of the pipe: Comparison of the mixture nanofluid model and experiment is shown: a. For 1% TiO$_2$; b. For 2.5% TiO$_2$.
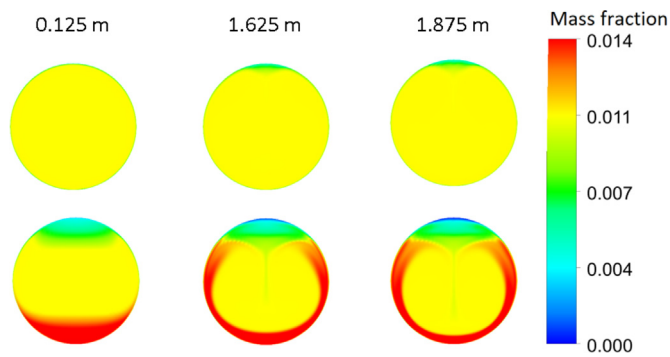
Fig. 20. Nanoparticle mass fraction at three cross-sections along the pipe. Top row: Case 1, bottom row: Case 2.
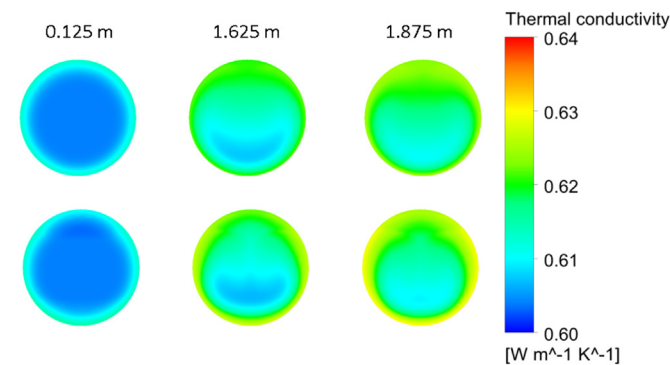
Fig. 21. Nanofluid thermal conductivity at three cross-sections along the pipe. Top row: Case 1, bottom row: Case 2.

the material properties, which reproduced the tabulated data in [35] with a better precision. For both sets of material properties the data could not be matched any better through the addition of a run-out, or through meshing the wall manually. The simplest geometric model will suffice for further simulations. As a conclusion, the second set of material properties led to a much better matching of experiment and simulation.

4.3. Model validation for each numerical test

The model validation was accomplished by preliminary simulations on water flow in a validated mesh. The water thermophysical properties' approach for each numerical test are detailed in Tables 5–8 [12,27,35–39].

The numerical model validation was achieved after comparing data

a.   b.
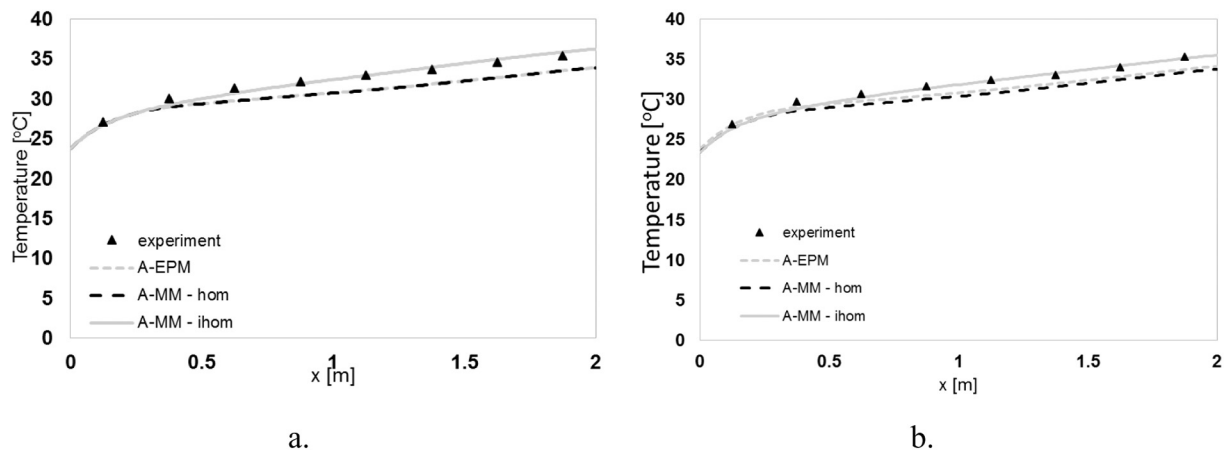
Fig. 22. Comparison of single phase and mixture nanofluid models: a. For 1% TiO$_2$; b. For 2.5% TiO$_2$.
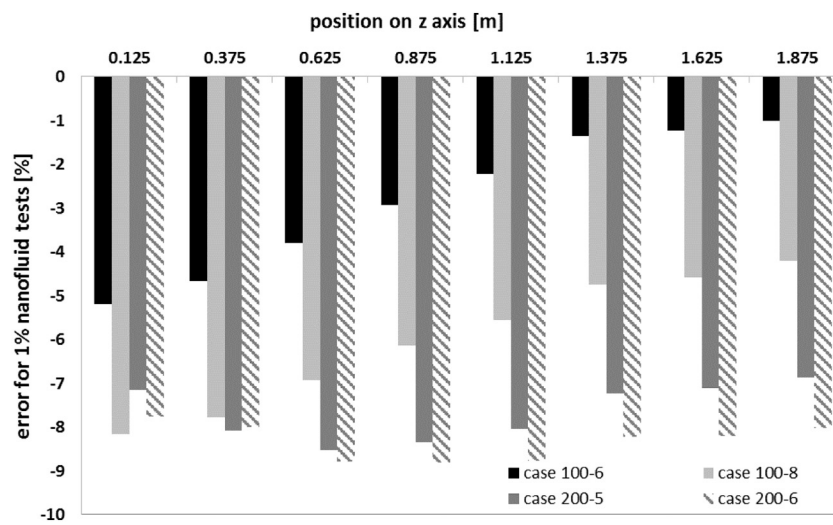
Fig. 23. Results for 1% titania nanofluid.
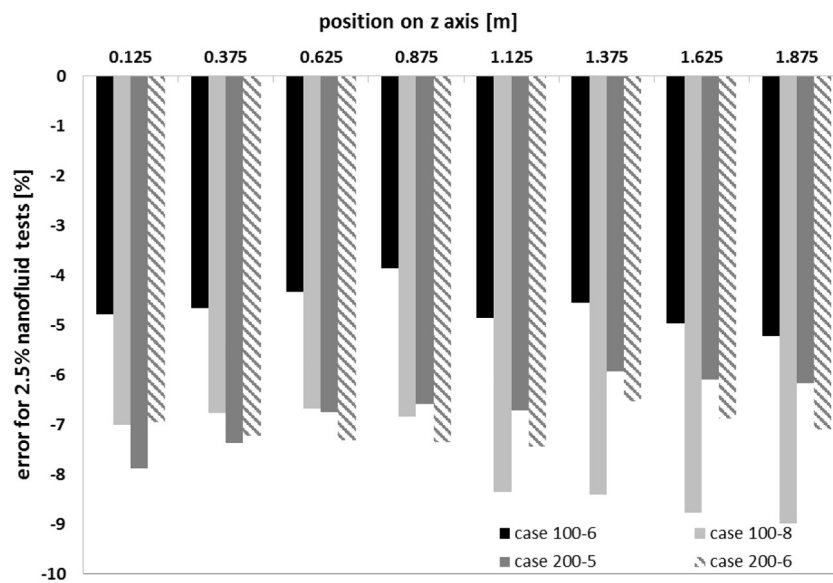
Fig. 24. Results for 2.5% titania nanofluid.
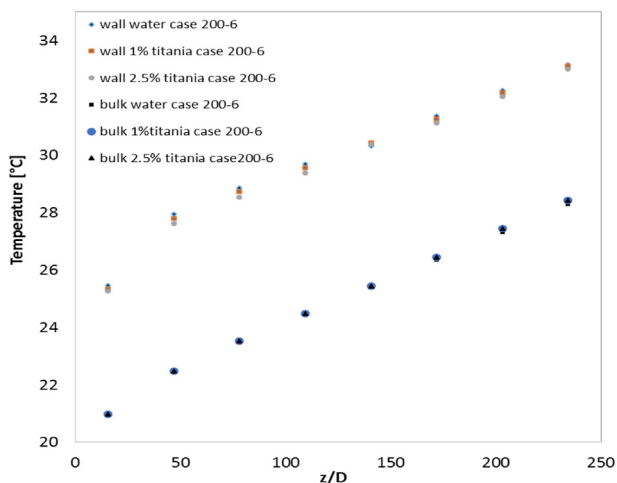
Fig. 25. Effect of nanoparticle concentration on the temperature axial distributions for Case 200-6.

for water with the experimental results performed by Colla et al. [26]. Results are depicted in Table 9, for test case 100–8, as defined in Appendix A.

5. Results and discussion on water flow

Results for each test case will be discussed separately in this section.

5.1. Test A

In the following we provide an analysis for the 200 W, 6 g/s test case. Looking at the temperature field in Fig. 9, we observe the development of a vertical temperature gradient, which is caused by natural convection. As the cold fluid enters the heated pipe, it is warmed at the walls and, due to density differences, natural convection develops in the form of two counter rotating vortices stretching along the pipe.

5.2. Test B

Test B considered the water flow in laminar regime inside the meshed pipe model presented earlier in Fig. 4. The set-up of the numerical model was outlined in Table 3, and tests were conducted for two major situations: With and without shell conduction.

The error between the measured and simulated temperature is defined as:
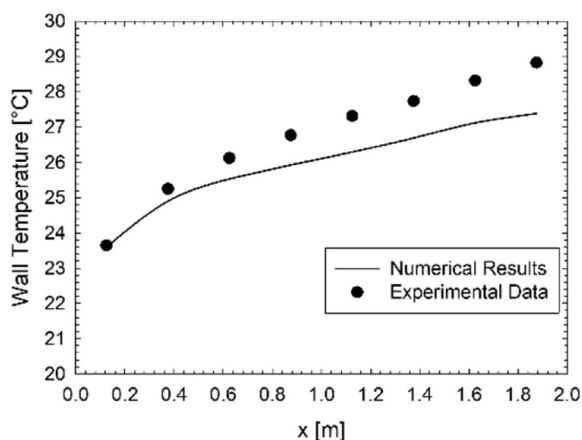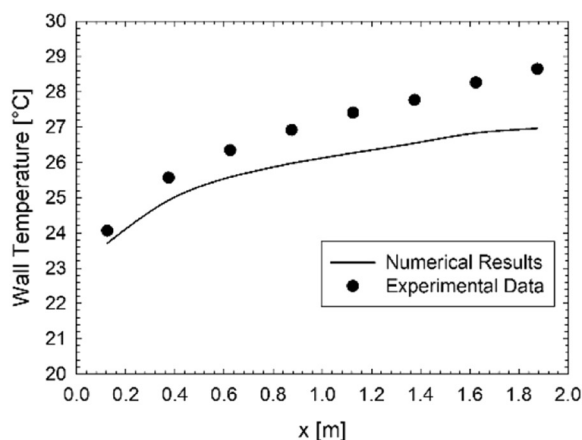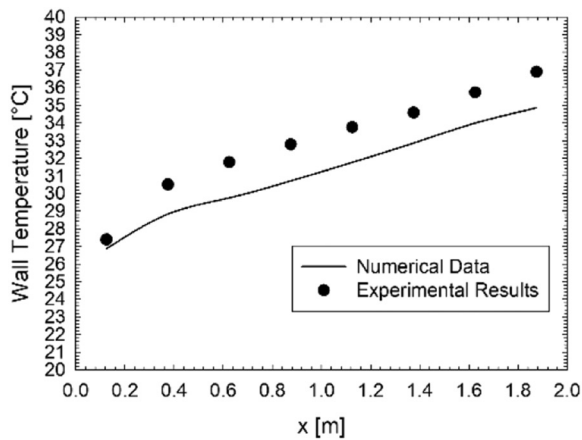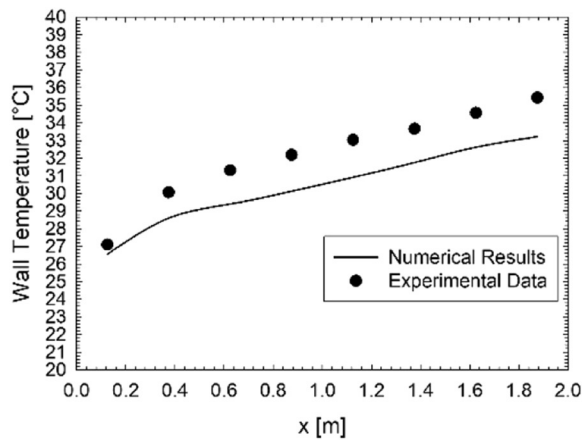
Fig. 26. Comparison in terms of wall temperature for different cases: a. Case 100-6; b. Case 100-8; c. Case 200-5 and d. Case 200-6 for 1% titania nanofluid.
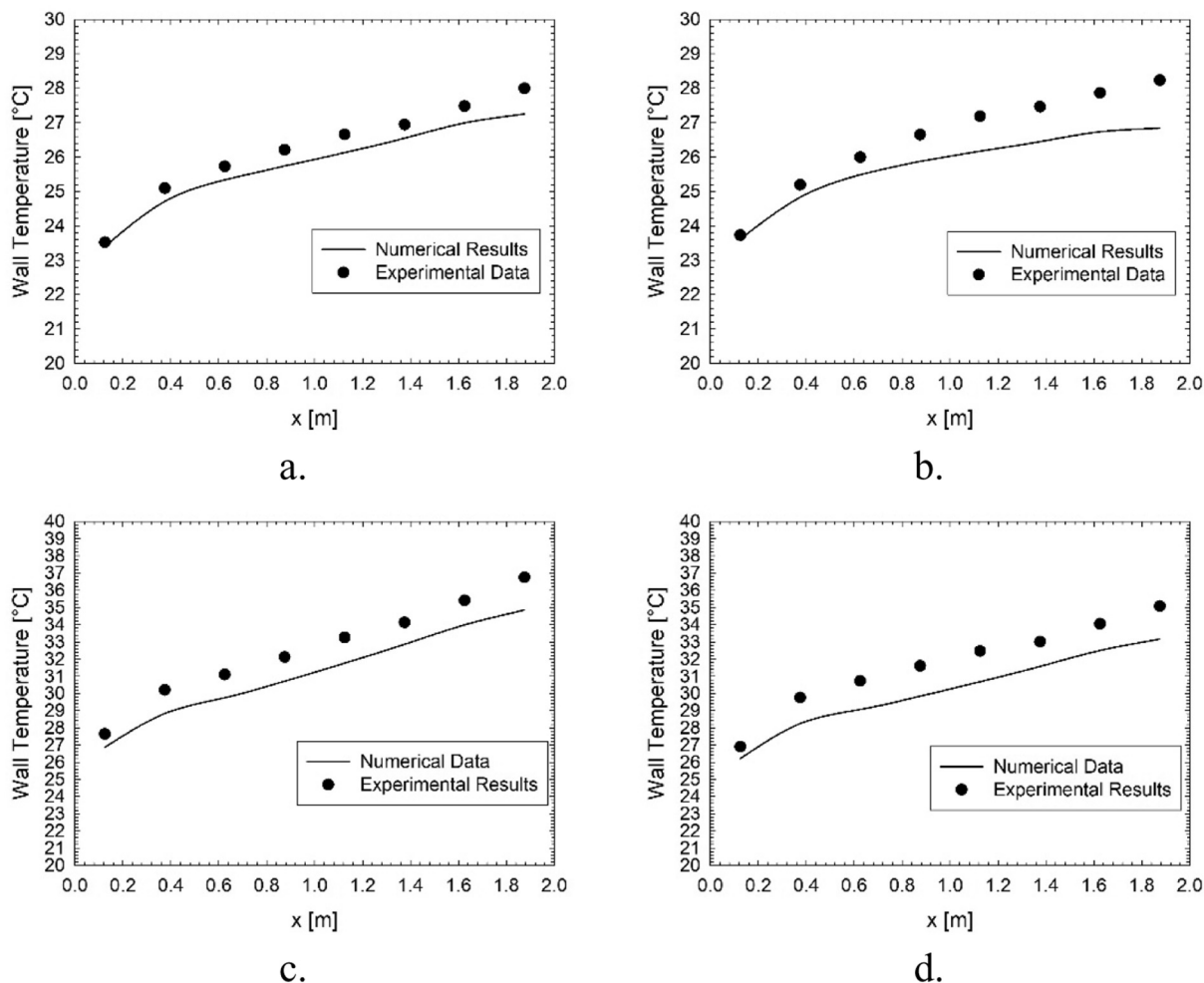
Fig. 27. Comparison in terms of wall temperature for different cases: a. Case 100-6; b. Case 100-8; c. Case 200-5 and d. Case 200-6 for 2.5% titania nanofluid.
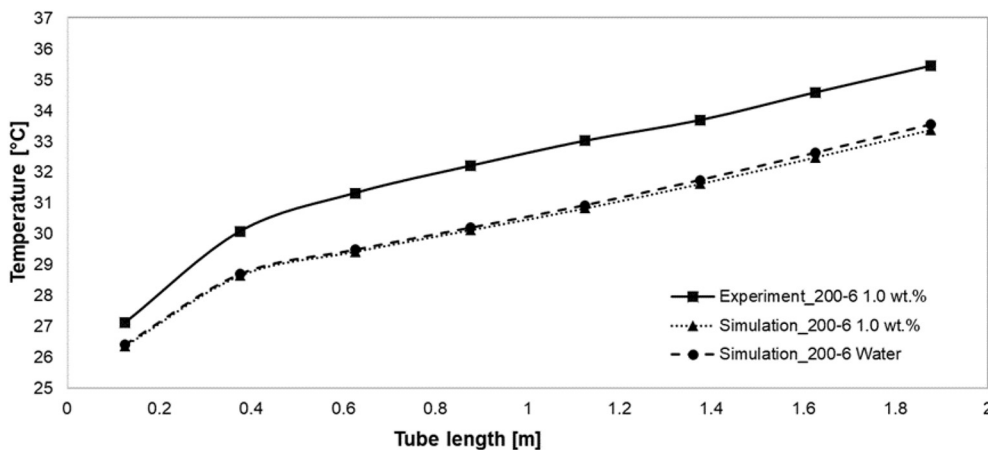
Fig. 28. Single phase simulation results of the 1% nanofluid (case: 200-6).

$$e(T) = 100 \left(\frac{T_{\exp erimental} - T_{numerical}}{T_{\exp erimental}} \right)$$

(32)

Thus, the case with no shell conduction was chosen for further simulations. Fig. 10 depicts the error obtained for no-shell conduction cases for all the performed tests. One can notice that the numerical results are constantly under-predicting the experimental ones, with a maximum error of 5%. The error was decreasing through the pipe exit and for higher heat flux. Nevertheless, all the test B results for water

were validated against the experimental values.

5.3. Test C

The results concerning the temperature variation along the tube, without gravity and with gravity, are shown in Table 9. Also, Figs. 11 and 12 depict the variation of the temperature in several cross-sections of the tube and the aspect of streamlines for both cases studied, with buoyancy effect (left) and without it (right). The maximum deviations
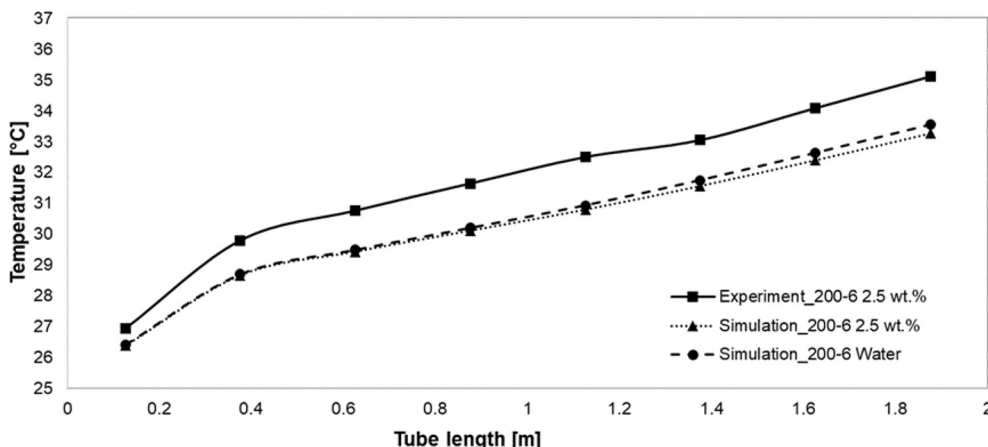
Fig. 29. Single phase simulation results for the 2.5% nanofluid (case: 200-6).
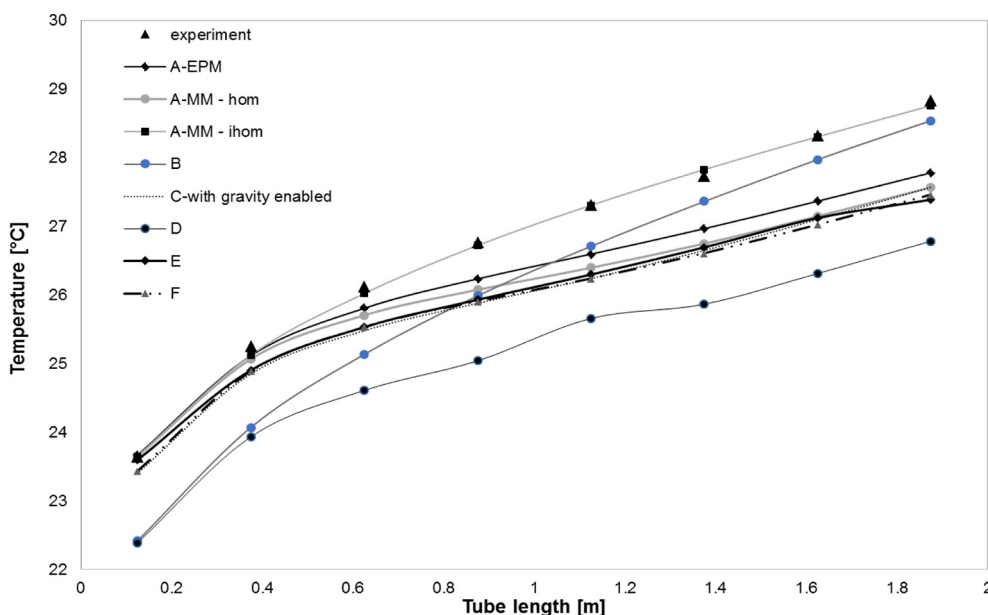
Fig. 30. Results for case 100-6 for 1% titania – water nanofluid.

of the CFD results were 0.5% for the cases with gravity and 7% for the simulations without gravity, which show that heat transfer in laminar flow is influenced significantly by mass forces.

As stated by Colla et al. [26], Fig. 12 reveals that mixed convection occurs, which leads to a swirling flow, and, finally, to an increased heat transfer.

5.4. Test D

In order to quantify the effect of the mass flow rate on the heat transfer performance of water, the axial distribution for both wall and bulk temperatures at P = 100 W and $\dot{m}$ = 6 and 8 g/s are plotted in Fig. 13. Both temperatures increased from inlet to outlet of the pipe. One can observe that the difference between wall and bulk temperatures at $\dot{m}$ = 8 g/s is slightly smaller than that for $\dot{m}$ = 6 g/s. This indicates that the heat transfer coefficient increases with the increase of the mass flow rate.

Fig. 14 displays the water temperature contours at three axial positions: z = 0.125 m, z = 1.125 m and z = 1.875 m for P = 100 W and $\dot{m}$ = 6 g/s. When the fluid moves further downstream, the circumferential wall temperature appears to be distributed non-uniformly in the

tangential direction, with a maximum temperature at the top of the tube. The warm fluid rises up to the upper half of the tube due to the buoyancy force inducing a stratification of the fluid temperature [40]. Note that the same behaviour is observed for the three other cases.

5.5. Test E

The results for water flow are in terms of bulk temperature and heat transfer coefficient for the 4 cases illustrated in Annex 1.

The bulk temperature was calculated as:

$$T_{bulk} = \frac{\int_A c_p \rho v T \, dA}{\int_A c_p \rho v \, dA}$$

(33)

where A is the cross-section of the pipe, ρ is the density of the fluid, v the axial velocity and T the local temperature. Results are presented in Figs. 15 and 16.
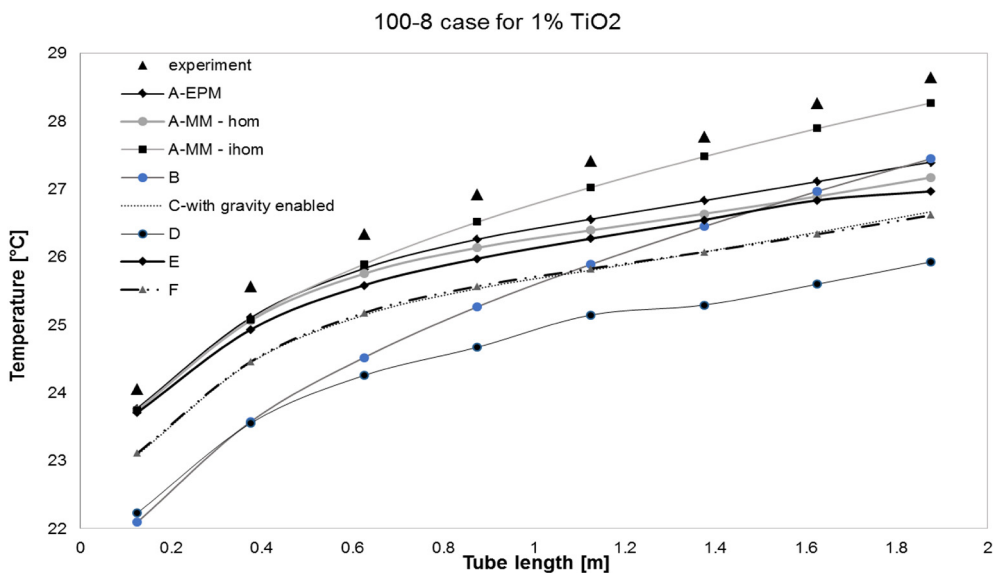
Fig. 31. Results for case 100-8 for 1% titania – water nanofluid.
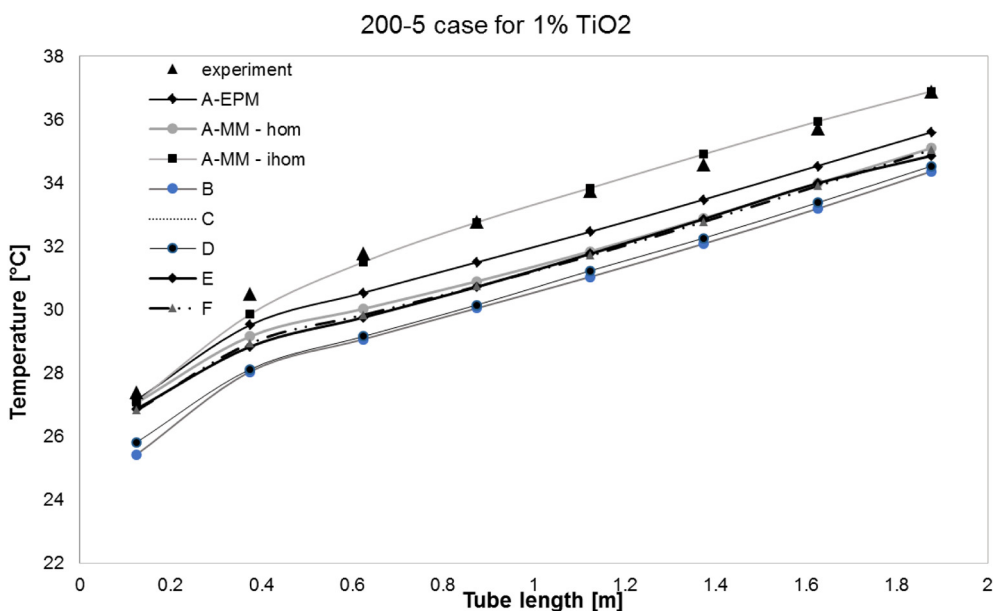
Fig. 32. Results for case 200-5 for 1% titania – water nanofluid.

5.6. Test F

The first set of water simulation results and its convergence study showed noticeable deviation from the experimental values. Therefore, the material properties were analysed for their precision and reproducibility, as shown in the last section. These revised material properties yielded better results, and were implemented for further simulations. The negligible difference in the temperature values of different cases (meshed wall, no meshed wall, run-out, no run-out) infers that the simplest solution (no meshed wall, no run-out) is adequate to replicate the experimental values, and can be applied for further simulations.

The water simulation results with different boundary conditions are shown in this section. Four simulations were run with the power input and inlet velocity as the only manipulative variables in every simulation case. All other factors were kept constant. The simulation results in comparison with the experimental values are illustrated in Figs. 17 and 18.

Based on Fig. 17, it can be observed that, in both simulation cases,

the experimental values could be reproduced with minimal deviations, with the highest temperature deviation of 0.13 K. The simulation results for Q = 200 W in Fig. 18 also exhibit the same behavior, and the maximum temperature deviations were computed at 0.24 K.

Overall, it can be concluded that the 3D simulation approach was successful in reproducing the experimental values with minimal differences.

6. Results and discussion on nanofluid flow

The results for this benchmark study will be discussed for each test case worked by every research group.

6.1. Test A

We continue our analysis for the 200–6 test case using the mixture nanofluid model. When employing the mixture model, one needs an additional boundary condition, namely the particle concentration
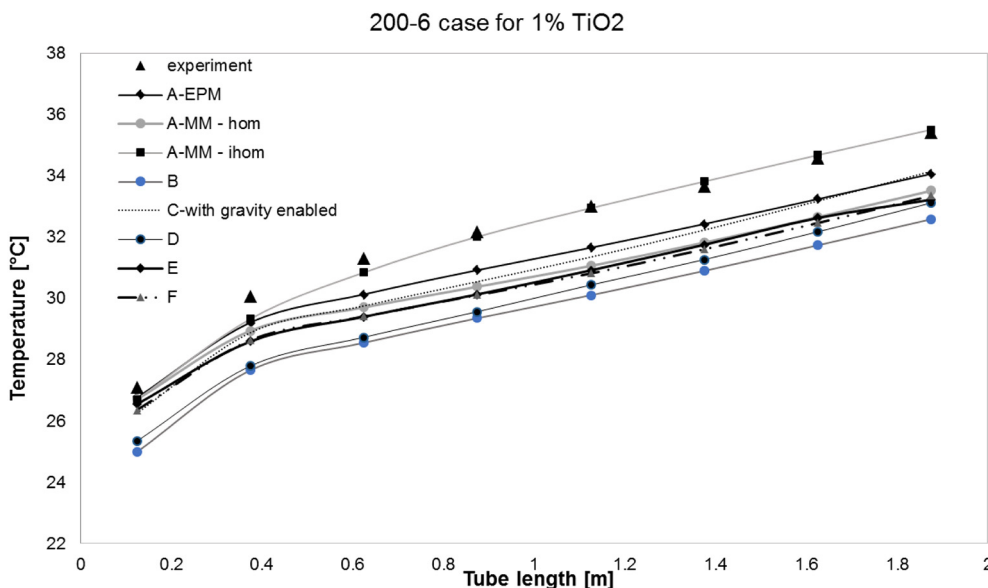
Fig. 33. Results for case 200-6 for 1% titania – water nanofluid.

Table 1
Thermal conductivity measurements [26,27].

Temperature, °C	Measured thermal conductivity, W/mK		
	Base fluid, [25]	Nanofluid with 1%wt. titania	Nanofluid with 2.5%wt. titania
10.3	0.581	0.570 ± 0.029	0.583 ± 0.029
20.4	0.599	0.598 ± 0.030	0.589 ± 0.029
30.5	0.616	0.619 ± 0.031	0.628 ± 0.031
40.5	0.631	0.641 ± 0.032	0.639 ± 0.032
50.5	0.644	0.667 ± 0.033	0.667 ± 0.033
60.3	0.655	0.698 ± 0.035	0.705 ± 0.035

Table 2
Viscosity measurements [26,27].

Temperature, °C	Measured viscosity, Pa s		
	Base fluid, [27]	Nanofluid with 1% wt. titania	Nanofluid with 2.5% wt. titania
10.0	0.001320	0.001306	0.001375
20.0	0.001023	0.001002	0.001025
30.0	0.000793	0.000797	0.000792
40.0	0.000645	0.000653	0.000661

distribution at the inlet of the pipe. We considered two cases, a homogenous inlet distribution (Case 1), and an inhomogeneous one, with a higher concentration of particles in the lower portion of the pipe (Case 2). Looking at the results of simulations, it can be noticed that homogenous particle concentration inlet yields results which are similar to the single phase model. This is due to the fact that the pipe is relatively short, and the effect of Brownian diffusion and thermophoresis are unable to produce large nanoparticle concentration differences, and, thus, results remain similar to the single-phase model. However, in Case 2, where the concentration of particles features a gradient at the entrance of the pipe, the results differ quite strongly.

In Fig. 19 we compare simulated temperature profiles along the wall of the pipe with experimental values. A good agreement with experimental results in the inhomogeneous inlet case was observed, while results are poor in the homogenous inlet case.

In Figs. 20 and 21 we show the contours of nanoparticle mass fraction and resulting nanofluid thermal conductivity at three cross-sections across the pipe. In Case 1, only small mass fraction and thermal conductivity variations can be seen across the pipe. There is simply not enough flow travel time through the pipe for the natural convection, thermophoresis and Brownian motion to generate a particle concentration gradient. This small variation results in the results of the Case 1 mixture model being very similar to the results of the single-phase model. In Case 2, it can be seen that the particle mass fraction (and, subsequently, the nanofluid properties), are changed significantly in the region along the walls of the pipe. The higher the concentration of nanoparticles is close to the walls, results in higher thermal conductivity and, finally, a higher temperature of the wall, which corresponds well to the experimental observations.

Finally, Fig. 22 compares wall temperature profiles with experiments for all developed models, and a good agreement was noticed with the mixture model with inhomogeneous inlet particle concentration, and poor agreement for the single phase and mixture models with homogenous inlet particle concentration.

6.2. Test B

In regard to Case B, the first important step in simulating the nanofluids flow was to consider the thermophysical properties appropriately. Some of these properties were determined determined experimentally by Cola et al. [26] at different temperatures. The procedure followed by Case B was to introduce these properties as a piecewise linear variation, since all thermophysical properties of any material usually have a linear modification over temperature. So, data from Tables 1 and 2 were introduced into the Ansys Fluent database. For the specific heat and density of the nanofluids both experimental and theoretical data were considered, as also were the suggestions from Colla et al. [26].

Figs. 23 and 24 depicts the data obtained from simulation in comparison with experimental data from Appendix A. It can be noticed that the errors in comparison with water flow are relatively high, but less than an acceptable error of 10%. Errors might appear from measurements of the thermophysical properties and their accuracy. Plus, the densities and specific heat of the nanofluids were not determined accurately experimentally for each nanofluid, and this might also introduce errors in the numerical approach.

As an overall comment, test B results are under-predicting the experimental determined temperatures constantly, with a maximum deviation of 9% at the exit, and this may lead to an increased heat transfer

Table 3
Overall description of test cases.

	Test A	Test B	Test C	Test D	Test E	Test F
Organisation/ contact person	University of Maribor, Slovenia / Prof. J. Ravnik	Technical University "Gheorghe Asachi" from Iasi, Romania / Prof. A.A. Minea	Transilvania University of Brasov, Romania / Prof. A. Huminic	Université de Sherbrooke, Canada / Prof. S. Poncet	Università degli Studi della Campania "Luigi Vanvitelli" Italy / Prof. O. Manca	University of Applied Sciences, Germany / Prof. P. Farber
CFD code	CFX Ansys	Fluent Ansys	CFX Ansys	Fluent Ansys	Fluent Ansys	Fluent Ansys
Flow conditions	3D laminar	3D laminar	3D laminar	3D laminar	3D laminar	3D laminar
Fluid assumptions	Single phase	Single phase	Single phase	Mixture model (two phase flow)	Mixture model (two phase flow)	Single phase flow
Boundary conditions	UDF for properties, based on experimental results	UDF for properties, based on experimental results	UDF for properties, based on experimental results	UDF for properties, based on experimental results	UDF for properties, based on experimental results	Temperature dependent functions, based on experimental results
Inlet conditions	UDF for developed velocity profile	Constant velocity profile	UDF for developed velocity profile	Constant velocity profile	UDF velocity profile	Constant velocity profile
Other conditions	gravity on y	– Gravity on y – No shell and shell conduction enabled	– Gravity on y – Conduction on tube wall (extra grid built for walls)	– Gravity on y – Shell conduction enabled – Population balance model to account for a more realistic nanoparticle size distribution	– Shell conduction activated	– Gravity on y – Shell conduction activated

Table 4
Wall and bulk temperatures obtained by the present numerical model for test case W-200-6. Comparisons between the experimental results and the numerical model with shell conduction for mesh grids.

x/D	Location	Experimental values for temperatures, ^0C	Relative error between the simulations and the experimental results (%) for the 5 mesh grids (in million nodes)				
			4	6	8	17	53
15.625	Wall	26.70	16.25	16.12	16.04	15.88	14.79
	Bulk	20.86	6.96	6.89	6.83	6.76	6.16
46.875	Wall	28.97	17	17.05	17.06	17.01	16.91
	Bulk	21.87	13.55	13.52	13.54	13.5	13.34
78.125	Wall	29.66	19.16	19.19	19.18	19.11	19.07
	Bulk	22.96	16.23	16.24	16.15	16.17	16.06
109.375	Wall	30.39	20.93	20.95	20.95	20.95	20.98
	Bulk	24.01	18.79	18.69	18.69	18.74	18.66
140.625	Wall	31.19	22.81	22.82	22.81	22.82	22.88
	Bulk	25.01	21.99	21.39	21.34	21.42	21.42
171.875	Wall	31.88	25.65	25.64	25.63	25.63	25.74
	Bulk	25.98	24.38	24.36	24.34	24.29	24.4
203.125	Wall	32.89	27.38	27.36	27.35	27.35	27.49
	Bulk	26.99	27.06	27.02	27.03	26.9	27.06
234.375	Wall	33.86	29.24	29.21	29.21	29.2	29.81
	Bulk	28.00	29.52	29.44	29.31	29.47	29.58

coefficient evaluated by numerical analysis in comparison with the experimental approach.

6.3. Test C

Similar simulations as were shown previously for Case C were performed for cases when nanofluid was considered, which was modelled as a single phase fluid using the properties shown in Tables 1 and 2. Based on the simulation concerning the base fluid, the gravity (see Table 9) depicts the average temperature along the tube for each studied case. As a conclusion, CFD results are lower than the experimental ones, maximum relative deviation being smaller than 7%, in the case of Ti 1%, $P = 100\,W$ and mass flow rate of 8 g/s.

6.4. Test D

The nanofluid flow was simulated by using the mixture model that treats the nanofluid as a single-phase fluid consisting of two strongly coupled phases. It solves the conservative equations of mass, momentum and energy for the mixture. However, each phase may have its own velocity. The thermophysical properties of the mixture are deduced from the weighted functions, depending on the properties of the two phases, weighted by their respective phase volume fractions. The model also accounts for the drag produced by the nanoparticles. The governing equations of the mixture model can be found in Buck et al. [41] and Song et al. [42]. The physical properties of water are considered to be temperature-dependent (Table 6), while those of the TiO_2 nanoparticles are kept constant.

Fig. 25 illustrates the axial distribution of both wall and bulk temperature for three nanoparticle concentrations at $P = 200\,W$ and $\dot{m} = 6\,g/s$. For this concentration range, adding nanoparticles to the base fluid decreased the temperature difference slightly between the heated wall and the bulk fluid, resulting in a better heat transfer. For instance, at $\varphi = 2.5$ wt%, the average difference between the wall and the bulk temperatures decreased by about 6.2% compared to the base fluid. Similar results are found for the other considered heat fluxes and mass flow rates, but, only the 200–6 case is discussed for the sake of brevity.

Adding nanoparticles to a base fluid not only enhances the transport properties of the mixture, but may also raise other phenomena, such as agglomeration, coagulation and sedimentation. Therefore, the stability

Table 5
Water thermophysical properties used for Tests A, B and C [36].

Property/equation	Eq. no.
Density [kg/m³]: $\rho(T) = 1.31839028583 \cdot 10^{-9} \cdot T^5 - 4.14156913208079 \cdot 10^{-7} \cdot T^4 + 0.0000627465524729587 \cdot T^3 - 0.0081245726054817 \cdot T^2 + 0.554068116720146 \cdot T + 999.9083719573 6$	(16)
Thermal conductivity [W/mK]: $k(T) = -0.000000000743543797 \cdot T^5 + 2.4371763574 \cdot 10^{-9} \cdot T^4 - 0.0000028899676105 67 \cdot T^3 + 5.15309471096903 \cdot 10^{-6} \cdot T^2 + 0.0018526713127628 4 \cdot T + 0.561293060017584$	(17)
Specific heat at constant pressure [J/kgK]: $c_p(T) = -4.08855065 3591 \cdot 10^{-8} \cdot T^5 + 0.0000117146192195605 \cdot T^4 - 0.0013771209563628 9 \cdot T^3 + 0.0902711920148249 \cdot T^2 - 2.9950083226021 9 \cdot T + 4217.11488982432$	(18)
Viscosity [Pas]: $\mu(T) = 2.414 \cdot 10^{-5} \times 10^{247.8/(T+133.15)}$	(19)

of nanofluids is a major problem, hindering their shelf life and their industrial applications. In recent decades, a significant amount of experimental studies have been conducted to evaluate the nanoparticles' agglomeration, dispersion and stability behaviour [43–45].

In the present case, the agglomeration phenomenon of nanoparticles was analysed numerically by evaluating the nanoparticle size and volume fraction distribution. To this end, a number density function was introduced to account for the nanoparticle distributions. The governing equation which describes the evolution of particle size distribution, in general, is called a population balance equation, and it is given as follows [45]:

$$\frac{\partial n(t,x)}{\partial t} + \frac{\partial [G(t,x)n(t,x)]}{\partial x} = A_{agg}(t,x) + N_{nuc}(t,x) + B_{break}(t,x)$$

$$(34)$$

where $n(t,x)$, $G(t,x)$, $A_{agg}(t,x)$, $N_{unuc}(t,x)$ and $B_{break}(t,x)$ are the number density, the growth term, the aggregation reaction term, the nucleation term and the breakage term, respectively.

This concept is referred to in general as the Population Balance Model, PBM, and it is based on the assumption that the particles of size x born (formed) when particles of sizes xi and xj aggregate, as well as the particles xi and xj die (vanish) via the volume balance, x is a function of xi and xj. The discrete phase model is used to model the TiO$_2$ agglomeration. The latter is based on representing directly the continuous Particles' Sizes Distribution (PSD) in terms of a set of discrete size classes or bins. The nanoparticles aggregate as a result of different acting forces, such as particle-particle interaction, diffusion force, thermophoresis and Brownian force. The random collision due to Brownian motion, in general, should not be avoided, especially in dispersed nanoparticles. Therefore, the free molecular aggregation Kernel model was used, where the frequency of nanoparticles' collision is size dependent, and it is defined as follow:

$$\beta(x_i, x_j) = \frac{2k_B T}{3\mu} \frac{(x_i + x_j)^2}{x_i x_j}$$

$$(35)$$

where k_B, T and μ are the Boltzmann constant, the absolute temperature and the host fluid viscosity, respectively. This frequency collision is also known as the Brownian kernel, or the perikinetic kernel.

In order to evaluate the effect of nanoparticle aggregation on the heat transfer rate, the average Nusselt number was calculated for Q = 200 W and $\dot{m}$ = 6 g/s. Two nanofluid concentrations were tested for both cases: With and without the Population Balance Model (PBM), as illustrated in Table 10. The latter shows clearly that, with these particular operating conditions, the agglomeration process has no effect on the thermal field throughout the domain.

6.5. Test E

The inlet region was not considered, and the velocity function was developed dynamically while the temperature was developing. The results are expressed in terms of wall temperature for different cases. In particular, for the nanofluid at 1%, the results are in Fig. 26.

The maximum deviation between the numerical model and the experimental data is about 5%.

For the nanofluid at 2.5% the results in terms of wall temperature are illustrated in Fig. 27 and the maximum deviation is about 5%.

More comparisons were carried out in terms of bulk temperature, heat transfer coefficient and Nusselt number for both nanofluids, and agreement was noticed.

6.6. Test F

The results from the single phase nanofluid simulations with different boundary conditions and their analysis are discussed in this section. The applied boundary conditions varied in terms of the power

Table 6
Water thermophysical properties used for Test D [12,37–39].

Property/equation	Eq. no.
Density (kg/m^3) [37]:	(20)
$\rho(T) = -2.0546 \cdot 10^{-10} \cdot T^5 + 4.0505 \cdot 10^{-7} \cdot T^4 - 3.1285 \cdot \cdot 10^{-4} \, T^3 + 0.11576 \cdot T^2$ $- 20.674 \cdot T + 2446$	
Specific Heat (J/kg K) [12]:	(21)
$c_p(T) = -4.088550653591 \cdot 10^{-8} \cdot T^5$ $+ 0.0000117146192195605 \cdot T^4 - 0.00137712095636289 \cdot T^3$ $+ 0.0902711920148249 \cdot T^2 - 2.99500832260219 \cdot T + 4217.11488982432$	
Thermal Conductivity (W/m K) [39]:	(22)
$k(T) = -0.98249 \; 10^{-5} \cdot T^2 + 7.535211 \cdot 10^{-3} \cdot T - 0.76761$	
Dynamic viscosity (Pa s) [38]:	(23)
$\mu(T) = A 10^{\left(\frac{B}{T-C}\right)}$, where A = 2.414 10^{-5}, B = 247.8 and C = 140	

Table 7
Water thermophysical properties used for Test E [27].

Property/equation	Eq. no.
Density (kg/m^3):	(24)
$\rho = 5.210 \cdot 10^3 + 0.8900 \cdot 10^2 T - 5.136 \cdot 10^{-1} T^2 + 1.499 \cdot 10^{-3} T^3 - 2.215 \cdot 10^{-6} T^4 + 1.318 \cdot 10^{-9} T^5$	
Specific Heat (J/kg K): $c_p = 1.672 \cdot 10^5 - 2.453 \cdot 10^3 T + 1.479 \cdot 10^2 T^2 - 4.468 \cdot 10^{-2} T^3 + 6.755 \cdot 10^{-5} T^4 - 4.088 \cdot 10^{-8} T^5$	(25)
Thermal Conductivity (W/m K):	(26)
$k = -1.13 + 9.71 \cdot 10^3 T - 1.31 \cdot 10^{-5} T^2$	
Dynamic viscosity (Pa s):	(27)
$\mu = 7.57 \cdot 10^{-2} - 6.37 \cdot 10^{-4} T + 1.80 \cdot 10^{-6} T^2 - 1.73 \cdot 10^{-9} T^3$	
The thermal conductivity of copper is considered constant, and it is: k_{Cu} = 401 W/m K	

Table 8
Water thermophysical properties used for Test F [35].

Property/equation	Eq. no.
Density (kg/m^3):	(28)
$\rho(T) = A + BT + CT^2 + DT^3 + ET^4$, where A = -413.15683, B = 13.27245, C = -0.040578, D = 0.000040, E = -2.27018×10^{-17}	
Specific Heat (J/kg K):	(29)
$c_p(T) = A + BT + CT^2 + DT^3 + ET^4$, where A = 6108.94345, B = -12.42600, C = 0.02000, D = $-5.540012 \times 10^{-17}$, E = $6.25929269271 \times 10^{-20}$	
Thermal Conductivity (W/m K):	(30)
$k(T) = A + BT + CT^2 + DT^3 + ET^4$, where A = -0.743567, B = 0.007513, C = -9.999999×10^{-6}, D = $-8.6331959 \times 10^{-18}$, E = 7.301424×10^{-21}	
Dynamic viscosity (Pa s):	(31)
$\mu(T) = A + BT + CT^2 + DT^3 + ET^4$, where A = 1.055787, B = -0.0132897, C = 0.00006309, D = $-1.33730666 \times 10^{-7}$, E = $-1.066666 \times 10^{-10}$	
The thermal conductivity of copper was modelled as a linear relationship between the following data points: k_{Cu} = 401 W/m K at 0 °C and k_{Cu} = 385 W/m K at 100 °C.	

Table 9
Model validation.

Position on the tube, as defined in Fig. 1		Experimen-tal values, °C	Error between simulation and experimental results, %							
Point	Distance, mm		Test A	Test B without shell	Test B with shell	Test C without gravity	Test C with gravity	Test D	Test E	Test F
P1	0.125	23.04	0.08	−4.04	−4.08	0.04	0.04	−3.42	2.89	0.40
P2	0.375	24.45	−0.19	−3.56	−3.59	−0.25	−0.05	−3.44	1.09	0.16
P3	0.625	25.08	0.16	−2.84	−2.92	0.17	1.17	−2.95	0.75	0.52
P4	0.875	25.47	0.13	−2.57	−2.80	0.11	2.50	−2.81	0.50	0.50
P5	1.125	25.79	−0.07	−2.58	−2.96	−0.08	3.68	−2.77	0.33	0.28
P6	1.375	26.04	−0.05	−2.42	−2.92	−0.08	4.88	−2.55	0.44	0.29
P7	1.625	26.43	−0.50	−2.75	−3.34	−0.52	5.31	−2.84	0.09	−0.16
P8	1.875	26.76	−0.66	−2.85	−3.47	−0.66	5.84	−2.86	−2.93	−0.32

Table 10
Averaged Nusselt number for two nanoparticle concentrations: 2.5%wt. and 4% wt. with and without PBM.

	Without PBM	With PBM
2.5% wt.	7.87	7.9
4% wt.	8.1	8.12

input, Q and inlet velocity. Eight simulation cases were conducted with two different weight percentages of nanoparticles (1.0% and 2.5%). As an example for the general results, two single phase nanofluid simulations (case 200-6, 1.0% and 2.5%) are illustrated and analysed in this section. The simulation results were compared to the experimental nanofluid results and the validated water simulation results.

The results for the simulations with 1.0% are shown in Fig. 28.

The simulated wall temperatures of the nanofluid are very close to

those of the water simulations, and a significant deviation can be observed from the experimental measured values of the nanofluids. The mean deviation between simulated and experimental values for the nanofluids is 1.8 K and the maximum 2.2 K. The temperature difference rises slightly up to measuring point 4, and then remains almost constant with a fluctuation of 0.1 K. The comparison between the water simulations and those of the nanofluids shows a mean deviation of 0.095 K and the maximum 0.175 K. The temperature difference increased slightly with increasing run length.

The results for the simulation with 2.5% are shown in Fig. 29.

The simulations with 2.5% show the same qualitative behaviour as with 1.0%. The average temperature difference between water simulations and single phase nanofluid simulations is 0.135 °C and, thus, slightly higher than at 1.0%. A comparison of the results between simulated and experimental values for the nanofluid shows that the mean deviation of 1.41 K is slightly below the values for 1.0%.

Overall, in all tested cases, the single phase simulations of the nanofluids have converged, but could not reproduce the experimental data. Rather, the results show that there is a high qualitative and quantitative similarity to the validated water simulations. The experimental results for the nanofluids show a reduction of the heat transfer between wall and fluid compared to the water experimental results [26] and single phase nanofluid simulations. Interactions between nanoparticles and fluid, e.g. Brownian molecular motion and thermophoretic forces, seem to have been the main drivers for this behaviour [29]. These effects cannot be demonstrated in single phase simulations and, therefore, support this thesis. The small deviations between simulated values for the nanofluid and water are due to the slightly changed material data for the nanofluid. In summary, the results show that two-phase simulations are probably necessary to reproduce the experimental results.

7. Overall results

This section is dedicated to the overall results in terms of accuracy of the numerical approach in comparison with the experimental results. Despite each test case individual description and assumptions, the results are presented in Figs. 30–33 for the nanofluid with 1%wt. TiO_2.

As one can see from the overall results, the model used for Case A and the mixture model with inhomogeneous inlet particle distribution get the best prediction, while the worst one was attained by Test D. Nevertheless, from the error calculus, it can get an error of 5–7% of Test

D if compared with the experimental outcomes.

Similar results were obtained for the 2.5% TiO_2 nanofluid, where the maximum error was 9% for Tests B and D, performed for case 100-8. The error upsurge was noticed when the heating flux was increasing.

8. Conclusion

An international nanofluid Round Robin exercise was conducted by 6 research groups participating from around the world. The aim of this benchmark study was to compare different approaches in numerical simulation while comparing the results with a very meticulous experimental study.

The key outcomes of this study are as follows:

1. The numerical approach using computational fluid dynamics approach is a very good tool to predict nanofluids' behavior at heat transfer, as well as the convection efficiency.
2. Data from all research groups are in the range of maximum −9% deviation from the experimental tests.
3. Most of the simulated temperatures are underpredicting the experimental results, thus, are slightly overpredicting the heat transfer efficiency.
4. Gravity has to be considered in all numerical approaches.
5. Some systematic differences were noticed when using the single phase approach, while the differences are in an acceptable interval, so the single phase approach can give reliable results only if the experimental thermophysical properties are considered.

In most engineering problems with complex physics and/or complex geometry, we would highly support the conclusion that a model is a good approach when the solution is going to a < 10% deviation, which would lead to the consequence that the single phase model would suffice. But, in this very simple geometry of a long straight pipe, a deviation of not > 3–5% would rather be reasonably expected. Consequently, the multiphase model can give the most trustable results when dealing with nanofluids' flow.

Acknowledgments

Appendix A. Detailed information about the proposed test cases

Test case 100-6 (P = 100 W, mass flow rate = 6 g/s)								
Power [W]								
0–1	1–2	2–3	3–4	4–5	5–6	6–7	7–8	8–9
6.322319	12.59909	12.579664	12.5910782	12.5030178	12.4486542	12.4342468	12.3888954	6.1899286
Water								
T_{in} [°C]		20.3094509714286						
T_{out} [°C]		24.3868722						
Mass flow rate $\left[\frac{kg}{s}\right]$		0.00597685714285714						
Average velocity $\left[\frac{m}{s}\right]$		0.119						
Measured wall temperature [°C]								
P1	P2	P3	P4	P5	P6	P7	P8	
23.3597	24.8623	25.4266	25.8084	26.1796	26.5495	27.0787	27.5752	
Water-TiO_2 1%								
T_{in} [°C]		20.66323924						
T_{out} [°C]		24.51104252						
Mass flow rate $\left[\frac{kg}{s}\right]$		0.0063018						
Average velocity $\left[\frac{m}{s}\right]$		0.124674714154704						
Measured wall temperature [°C]								
P1	P2	P3	P4	P5	P6	P7	P8	
23.6449	25.2503	26.1239	26.7715	27.3161	27.7386	28.3222	28.8308	

Water TiO$_2$ 2.5%

T$_{in}$ [^{o}C] 20.43895212
T$_{out}$ [^{o}C] 24.43862664
Mass flow rate $\left[\frac{kg}{s}\right]$ 0.00611704
Average velocity $\left[\frac{m}{s}\right]$ 0.119659774802486

Measured wall temperature [^{o}C]

P1	P2	P3	P4	P5	P6	P7	P8
23.5207	25.0956	25.7299	26.2127	26.6572	26.9448	27.4851	27.9988

Test case 100-8 (P = 100 W, mass flow rate = 8 g/s)

Power [W]

0–1	1–2	2–3	3–4	4–5	5–6	6–7	7–8	8–9
6.322319	12.59909	12.579664	12.591078	12.5030178	12.448654	12.434246	12.388895	6.1899286

Water

T$_{in}$ [^{o}C] 20.3284088285714
T$_{out}$ [^{o}C] 23.3899367428571
Mass flow rate $\left[\frac{kg}{s}\right]$ 0.00803194285714286
Average velocity $\left[\frac{m}{s}\right]$ 0.16

Measured wall temperature [^{o}C]

P1	P2	P3	P4	P5	P6	P7	P8
23.0410	24.4518	25.0778	25.4731	25.7917	26.0398	26.4263	26.7564

Water-TiO$_2$ 1%

T$_{in}$ [^{o}C] 21.05614052
T$_{out}$ [^{o}C] 23.9895748
Mass flow rate $\left[\frac{kg}{s}\right]$ 0.00832096
Average velocity $\left[\frac{m}{s}\right]$ 0.164619302918156

Measured wall temperature [^{o}C]

P1	P2	P3	P4	P5	P6	P7	P8
24.0600	25.5663	26.3458	26.9199	27.4113	27.7697	28.2657	28.6501

Water TiO$_2$ 2.5%

T$_{in}$ [^{o}C] 20.96067984
T$_{out}$ [^{o}C] 23.88210684
Mass flow rate $\left[\frac{kg}{s}\right]$ 0.00828512
Average velocity $\left[\frac{m}{s}\right]$ 0.162070494082999

Measured wall temperature [^{o}C]

P1	P2	P3	P4	P5	P6	P7	P8
23.7281	25.1942	25.9971	26.6499	27.1888	27.4644	27.8676	28.2351

Test case 200-5 (P = 200 W, mass flow rate = 5 g/s)

Power [W]

0–1	1–2	2–3	3–4	4–5	5–6	6–7	7–8	8–9
12.645252	25.199415	25.157642	25.183376	25.007246	24.898513	24.869698	24.77899	12.380457

Water

T$_{in}$ [^{o}C] 20.4072873142857
T$_{out}$ [^{o}C] 30.3567075714286
Mass flow rate $\left[\frac{kg}{s}\right]$ 0.00481022857142857
Average velocity $\left[\frac{m}{s}\right]$ 0.096

Measured wall temperature [^{o}C]

P1	P2	P3	P4	P5	P6	P7	P8
26.9659	29.1789	29.9926	30.9231	31.9541	32.9771	34.2216	35.4678

Water-TiO$_2$ 1%

T$_{in}$ [^{o}C] 20.72783032
T$_{out}$ [^{o}C] 30.17570772
Mass flow rate $\left[\frac{kg}{s}\right]$ 0.00506076
Average velocity $\left[\frac{m}{s}\right]$ 0.100192305013324

Measured wall temperature [^{o}C]

P1	P2	P3	P4	P5	P6	P7	P8
27.3851	30.5061	31.7774	32.7843	33.7539	34.5859	35.7339	36.8954

Water TiO$_2$ 2.5%

T$_{in}$ [^{o}C] 20.42931976
T$_{out}$ [^{o}C] 30.33637348
Mass flow rate $\left[\frac{kg}{s}\right]$ 0.00483872
Average velocity $\left[\frac{m}{s}\right]$ 0.0947206421346319

Measured wall temperature [^{o}C]

P1	P2	P3	P4	P5	P6	P7	P8
27.6379	30.2110	31.1077	32.1243	33.2631	34.1295	35.4107	36.7575

Test case 200-6 (P = 200 W, mass flow rate = 6 g/s)								
Power [W]								
0–1	1–2	2–3	3–4	4–5	5–6	6–7	7–8	8–9
12.645252	25.199415	25.157642	25.183376	25.007246	24.898513	24.869698	24.77899	12.380457
Water								
T_{in} [°C]		20.4309997714286						
T_{out} [°C]		28.4802120857143						
Mass flow rate $\left[\frac{kg}{s}\right]$		0.00598191428571429						
Average velocity $\left[\frac{m}{s}\right]$		0.119						
Measured wall temperature [°C]								
P1	P2	P3	P4	P5	P6	P7	P8	
26.5189	28.8542	29.5711	30.3115	31.0724	31.8340	32.8079	33.7793	
Water-TiO$_2$ 1%								
T_{in} [°C]		20.83672112						
T_{out} [°C]		28.46655984						
Mass flow rate $\left[\frac{kg}{s}\right]$		0.0063294						
Average velocity $\left[\frac{m}{s}\right]$		0.12528311801163						
Measured wall temperature [°C]								
P1	P2	P3	P4	P5	P6	P7	P8	
27.0999	30.0663	31.3078	32.1889	33.0038	33.6719	34.5715	35.4285	
Water TiO$_2$ 2.5%								
T_{in} [°C]		20.42612872						
T_{out} [°C]		28.38385764						
Mass flow rate $\left[\frac{kg}{s}\right]$		0.00608732						
Average velocity $\left[\frac{m}{s}\right]$		0.119133590449441						
Measured wall temperature [°C]								
P1	P2	P3	P4	P5	P6	P7	P8	
26.8984	29.7629	30.7296	31.6093	32.4671	33.0164	34.05401	35.0789	

References

[1] S. Kumar, A. Kumar, A.D. Kothiyal, M.S. Bisht, A review of flow and heat transfer behaviour of nanofluids in micro channel heat sinks, Ther. Sci. Eng. Progr. 8 (2018) 477–493.

[2] G. Huminic, A. Huminic, Hybrid nanofluids for heat transfer applications – a state-of-the-art review, Int. J. Heat Mass Transf. 125 (2018) 82–103.

[3] H.J. Xu, Z.B. Xing, F.Q. Wang, Z.M. Cheng, Review on heat conduction, heat convection, thermal radiation and phase change heat transfer of nanofluids in porous media: fundamentals and applications, Chem. Eng. Sci. 195 (2019) 462–483.

[4] T. Ambreen, M.H. Kim, Heat transfer and pressure drop correlations of nanofluids: a state of the art review, Renew. Sustain. Energy Rev. 91 (2018) 564–583.

[5] R.V. Pinto, F.A.S. Fiorelli, Review of the mechanisms responsible for heat transfer enhancement using nanofluids, Appl. Therm. Eng. 108 (2016) 720–739.

[6] A. Alirezaie, M.H. Hajmohammad, A. Alipour, M. Salari, Do nanofluids affect the future of heat transfer? a benchmark study on the efficiency of nanofluids, Energy 157 (2018) 979–989.

[7] M. Raja, R. Vijayan, P. Dineshkumar, M. Venkatesan, Review on nanofluids' characterization, heat transfer characteristics and applications, Renew. Sustain. Energy Rev. 64 (2016) 163–173.

[8] R.B. Ganvir, P.V. Walke, V.M. Kriplani, Heat transfer characteristics in nanofluid—a review, Renew. Sustain. Energy Rev. 75 (2017) 451–460.

[9] V. Bianco, O. Manca, S. Nardini, K. Vafai, Heat Transfer Enhancement with Nanofluids, 1st edition, CRC Press, 2017.

[10] S.K. Das, S.U. Choi, W. Yu, T. Pradeep, Nanofluids: Science and Technology, Wiley, 2007.

[11] D.D. Ganji, A. Malvandi, Heat Transfer Enhancement Using Nanofluid Flow in Microchannels: simulation of Heat and Mass Transfer, William Andrew Publishing, 2016.

[12] A.A. Minea, Advances in New Heat Transfer Fluids: From Numerical to Experimental Techniques, 1st edition, CRC Press, 2017.

[13] W.H. Lee, et al., Round-robin test on thermal conductivity measurement of ZnO nanofluids and comparison of experimental results with theoretical bounds, Nanoscale Res. Lett. 6 (2011) 258.

[14] J. Buongiorno, et al., A benchmark study on the thermal conductivity of nanofluids, J. Appl. Phys. 106 (2009) 094312.

[15] A. Alirezaie, M.H. Hajmohammad, A. Alipour, M. Salari, Do nanofluids affect the future of heat transfer?" a benchmark study on the efficiency of nanofluids", Energy 157 (2018) 979–989.

[16] H. Xu, Z. Xing, K. Vafai, Analytical considerations of flow/thermal coupling of nanofluids in foam metals with local thermal non-equilibrium (LTNE) phenomena and inhomogeneous nanoparticle distribution, Int. J. Heat Fluid Flow 77 (2019) 242–255.

[17] H. Xu, L. Gong, S. Huang, M. Xu, Flow and heat transfer characteristics of nanofluid flowing through metal foams, Int. J. Heat Mass Transf. 83 (2015) 399–407.

[18] H. Xu, Z. Xing, The lattice Boltzmann modeling on the nanofluid natural convective transport in a cavity filled with a porous foam, Int. Commun. Heat Mass Transfer 89 (2017) 73–82.

[19] H.W. Chiam, W.H. Azmi, N.M. Adam, M.K.A.M. Ariffin, Numerical study of nanofluid heat transfer for different tube geometries – a comprehensive review on performance, Int. Commun. Heat Mass Transfer 86 (2017) 60–70.

[20] S.M. Vanaki, P. Ganesan, H.A. Mohammed, Numerical study of convective heat transfer of nanofluids: a review, Renew. Sustain. Energy Rev. 54 (2016) 1212–1239.

[21] A. Kamyar, R. Saidur, M. Hasanuzzaman, Application of computational fluid dynamics (CFD) for nanofluids, Int. J. Heat Mass Transf. 55 (2012) 4104–4115.

[22] S.K. Dewangan, Review of computational fluid dynamics (CFD) researches on nano fluid flow through micro channel, AIP Conf. Proc. 1953 (2018) 140036.

[23] A. Kamyar, R. Saidur, M. Hasanuzzaman, Application of computational fluid dynamics (CFD) for nanofluids, Int. J. Heat Mass Transf. 55 (2012) 4104–4115.

[24] O. Mahian, L. Kolsi, M. Amani, P. Estellé, G. Ahmadi, C. Kleinstreuer, J.S. Marshall, R.A. Taylor, E. Abu-Nada, S. Rashidi, H. Niazmand, S. Wongwises, T. Hayat, A. Kasaeian, I. Pop, Recent advances in modeling and simulation of nanofluid flows—part II: applications, Phys. Rep. 791 (2019) 1–59.

[25] O. Mahian, L. Kolsi, M. Amani, P. Estellé, G. Ahmadi, C. Kleinstreuer, J.S. Marshall, M. Siavashi, R.A. Taylor, H. Niazmand, S. Wongwises, T. Hayat, A. Kolanjiyil, A. Kasaeian, I. Pop, Recent advances in modeling and simulation of nanofluid flows-part I: fundamental and theory, Phys. Rep. 790 (2019) 1–48.

[26] L. Colla, L. Fedele, M.H. Buschmann, Laminar mixed convection of TiO2-water nanofluid in horizontal uniformly heated pipe flow, Int. J. Therm. Sci. 97 (2015) 26–40.

[27] E.W. Lemmon, M.L. Huber, M.O. McLinden, NIST Standard Reference Database 23, Reference Fluid Thermodynamic and Transport Properties (REFPROP), Version 9.0, National Institute of Standards and Technology, 2010.

[28] H.C. Brinkman, The viscosity of concentrated suspensions and solutions, J. Chem. Phys. 20 (1952) 571–581.

[29] K. Khanafer, K. Vafai, M. Lightstone, Buoyancy-driven heat transfer enhancement in a two-dimensional enclosure utilizing nanofluids, Int. J. Heat Mass Transf. 46 (2003) 3639–3653.

[30] J.C. Maxwell, A Treatise on Electricity and Magnetism, 2nd ed, Clarendon Press, Oxford, UK, 1881.

[31] D. Wen, Y. Ding, Experimental investigation into convective heat transfer of nanofluids at the entrance region under laminar flow conditions, Int. J. Heat Mass Transf. 47 (2004) 5181–5188.

[32] J. Buongiorno, Convective transport in Nanofluids, J. Heat Transfer 128 (3) (2006) 240.

[33] G. Huminic, A. Huminic, Numerical analysis of hybrid nanofluids as coolants for automotive applications, Int. J. Heat Technol. 35 (2017) 288–292.

[34] G. Huminic, A. Huminic, The heat transfer performances and entropy generation analysis of hybrid nanofluids in a flattened tube, Int. J. Heat Mass Transf. 119

(2018) 813–827.

[35] V.D. Ingenieure, VDI Gesellschaft verfahrenstechnik und, in: Chemieingenieurwesen (Ed.), VDI - Wärmeatlas, 10th edition, Springer-Verlag, Berlin, 2006.

[36] M. McLinden, E. Lemmon, M. Huber, NIST Standard Reference Database 23: Reference Fluid Thermodynamic and Transport Properties-REFPROP, Standard Reference Data Program, Technical Report, Gaithersburg, 2010.

[37] N. Vargaftik, Tables on the Thermophysical Properties of Liquids and Gases: In Normal and Dissociated States, Hemisphere Publishing Corporation, 1975.

[38] C.H. Chon, K.D. Kihm, S.P. Lee, S. Choi, Empirical correlation depending the role of temperature and particle size for nanofluid (Al2O3) thermal conductivity enhancement, Appl. Phys. Lett. 87 (2005) 153107.

[39] C. de Castro, S. Li, A. Nagashima, R. Trengove, W. Wakeham, Standard reference data for the thermal conductivity of liquids, J. Phys. Chem. Ref. Data Monogr. 15 (1986) 1073–1086.

[40] G. McNab, A. Meisen, Thermophoresis in liquids, J. Colloid Interface Sci. 44 (1973)

339–346.

[41] A. Bück, P. Mirko, N. Martina, T. Evangelos, Population balance model for drying of droplets containing aggregating nanoparticles, AICHE J. 58 (2012) 3318–3328.

[42] D. Song, J. Dengwei, G. Jiafeng, R. Yuxun, A modified aggregation based model for the accurate prediction of particle distribution and viscosity in magnetic nanofluids, Powder Technol. 283 (2015) 561–569.

[43] J.Z. Lin, X. Yi, K. Xiao-Ke, Pressure drop and heat transfer of nanofluid in turbulent pipe flow considering particle coagulation and breakage, J. Heat Transfer 136 (2014) 111701.

[44] S. Lopes, P. Proulx, J. Gouriet, P. Rambaud, Applcation of an integrated CFD model to aluminum nanoparticle production, Proc. of the 15th International Heat Transfer Conference, Kyoto, Japan, 2014, pp. 6465–6479.

[45] A. Majumder, K. Vinay, A. Santosh, R. Arvind, Lattice Boltzmann method for population balance equations with simultaneous growth, nucleation, aggregation and breakage, Chem. Eng. Sci. 69 (2012) 316–328.